The Prediction and Analysis of Jet Flows and Scattered Turbulent Mixing Noise about Flight Vehicle Airframes

Steven A. E. Miller
Langley Research Center, Hampton, Virginia

NASA STI Program . . . in Profile

Since its founding, NASA has been dedicated to the advancement of aeronautics and space science. The NASA scientific and technical information (STI) program plays a key part in helping NASA maintain this important role.

The NASA STI program operates under the auspices of the Agency Chief Information Officer. It collects, organizes, provides for archiving, and disseminates NASA's STI. The NASA STI program provides access to the NASA Aeronautics and Space Database and its public interface, the NASA Technical Report Server, thus providing one of the largest collections of aeronautical and space science STI in the world. Results are published in both non-NASA channels and by NASA in the NASA STI Report Series, which includes the following report types:

- TECHNICAL PUBLICATION. Reports of completed research or a major significant phase of research that present the results of NASA Programs and include extensive data or theoretical analysis. Includes compilations of significant scientific and technical data and information deemed to be of continuing reference value. NASA counterpart of peer-reviewed formal professional papers, but having less stringent limitations on manuscript length and extent of graphic presentations.

- TECHNICAL MEMORANDUM. Scientific and technical findings that are preliminary or of specialized interest, e.g., quick release reports, working papers, and bibliographies that contain minimal annotation. Does not contain extensive analysis.

- CONTRACTOR REPORT. Scientific and technical findings by NASA-sponsored contractors and grantees.

- CONFERENCE PUBLICATION. Collected papers from scientific and technical conferences, symposia, seminars, or other meetings sponsored or co-sponsored by NASA.

- SPECIAL PUBLICATION. Scientific, technical, or historical information from NASA programs, projects, and missions, often concerned with subjects having substantial public interest.

- TECHNICAL TRANSLATION. English-language translations of foreign scientific and technical material pertinent to NASA's mission.

Specialized services also include organizing and publishing research results, distributing specialized research announcements and feeds, providing information desk and personal search support, and enabling data exchange services.

For more information about the NASA STI program, see the following:

- Access the NASA STI program home page at *http://www.sti.nasa.gov*

- E-mail your question to help@sti.nasa.gov

- Fax your question to the NASA STI Information Desk at 443-757-5803

- Phone the NASA STI Information Desk at 443-757-5802

- Write to:
  STI Information Desk
  NASA Center for AeroSpace Information
  7115 Standard Drive
  Hanover, MD 21076-1320

The Prediction and Analysis of Jet Flows and Scattered Turbulent Mixing Noise about Flight Vehicle Airframes

Steven A. E. Miller
Langley Research Center, Hampton, Virginia

Acknowledgments

Abstract

Jet flows interacting with nearby surfaces exhibit a complex behavior in which acoustic and aerodynamic characteristics are altered. The physical understanding and prediction of these characteristics are essential to designing future low noise aircraft. A new approach is created for predicting scattered jet mixing noise that utilizes an acoustic analogy and steady Reynolds-averaged Navier-Stokes solutions. A tailored Green's function accounts for the propagation of mixing noise about the airframe and is calculated numerically using a newly developed ray tracing method. The steady aerodynamic statistics, associated unsteady sound source, and acoustic intensity are examined as jet conditions are varied about a large flat plate. A non-dimensional number is proposed to estimate the effect of the aerodynamic noise source relative to jet operating condition and airframe position. The steady Reynolds-averaged Navier-Stokes solutions, acoustic analogy, tailored Green's function, non-dimensional number, and predicted noise are validated with a wide variety of measurements. The combination of the developed theory, ray tracing method, and careful implementation in a stand-alone computer program result in an approach that is more first principles oriented than alternatives, computationally efficient, and captures the relevant physics of fluid-structure interaction.

Nomenclature

Symbols

A	Empirical constant
C	Diffraction coefficient for corner-diffracted rays
c	Speed of sound
c_l	Empirical constant associated with turbulent length scale
c_τ	Empirical constant associated with turbulent time scale
c_∞	Free-stream speed of sound
D	Nozzle exit diameter
D	Diffraction coefficient for edge diffracted ray
D_j	Fully expanded jet diameter
D_m	Diffraction coefficient for creeping ray
$\boldsymbol{E}^0$	First end point of edge segment
$\boldsymbol{E}^F$	Second end point of edge segment
f_1	First damping function of discontinuity correction
f_2	Second damping function of discontinuity correction
k	Wave number or turbulent kinetic energy (TKE)
k_s	Turbulent kinetic energy associated with fine-scale mixing noise
M_a	Acoustic Mach number
M_d	Design Mach number
M_j	Fully expanded Mach number
M_∞	Free-stream Mach number
$\boldsymbol{N}$	Axis of the diffraction cone and unit vector of edge
$\boldsymbol{O}$	Observer location
p	Static pressure
p_a	Acoustic pressure
p_j	Fully expanded static pressure
p_o	Stagnation pressure
$\hat{p}_D$	Complex pressure amplitude of diffracted ray
L	Length of plate used for point source validation
l_s	Turbulent length scale
$\hat{p}_I$	Complex pressure amplitude of incident ray
$\hat{q}_s$	Statistical source term
r	Distance from edge to observer
$\boldsymbol{S}$	Source location
S	Spectral density of acoustic pressure
St	Strouhal number
T	Transfer function used for creeping rays
T_j	Fully expanded static temperature
T_o	Stagnation temperature
t	Proportionate distance along edge segment
$\overline{u}$	Mean streamwise velocity component
u_j	Fully expanded jet velocity
$\boldsymbol{V}$	Diffraction location
W	Width of plate used for point source validation
$\boldsymbol{x}$	Vector observer position
x_I	Jet impingement location
x_p	Axial distance from the jet centerline to the plate
$\boldsymbol{y}$	Source vector
y_p	Radial distance from the plate to jet centerline
β	Wedge angle
δ	Damping coefficient of discontinuity correction
δ_{ij}	Kronecker delta function
δ_η	Spreading angle of the jet
Γ	Non-dimensional number
γ	Ratio of specific heats
ϕ_o	Polar angle of diffracted ray
ϕ_s	Polar angle of incident ray
Ψ	Observer angle from the upstream axis
ν	Wedge index
ρ	Density or Distance from source to observer
θ	Oblique angle between the edge and incident ray
τ_s	Turbulent time scale
ω	Radial frequency

Abbreviations

AMELIA	Advanced model for extreme lift and improved aeroacoustics
BBSAN	Broadband shock-associated noise
BVP	Boundary value problem
CFD	Computational fluid dynamics
CJES	Compact jet engine simulator
DNS	Direct numerical simulation
EPNL	Effective perceived noise level
ESM	Equivalent source method
FSC	Fast scattering code
FUN3D	Fully unstructured Navier-Stokes three-dimensional solver
HBPR	High bypass ratio
HWB	Hybrid-wing body
JSIT	Jet-surface interaction test
NPR	Nozzle pressure ratio
LEE	Linearized Euler equations
LBPR	Low bypass ratio
PIV	Particle image velocimetry
OASPL	Overall sound pressure level
PIV	Particle image velocimetry
PSD	Power spectral density
RANS	Reynolds-averaged Navier-Stokes
SHJAR	Small hot jet acoustic rig
SPL	Sound pressure level
SMC	Small metal chevron
SST	Shear stress transport
TTR	Total temperature ratio

1 Introduction

Jet powered flight vehicles generate high intensity acoustic radiation that has a negative impact on the surrounding community, military personnel, and can cause sonic fatigue. The need to reduce jet noise and its impact on the surrounding environment cause communities to create noise regulations. These restrictions have contributed to motivating the research and development of noise reduction technology. One such technology integrates the propulsion system with the flight vehicle airframe as shown by Hill and Thomas [1]. Envia and Thomas [2] outline the difficulties of reducing noise with continued airline traffic growth. Advanced aircraft configurations are required for continued noise reduction.

Examples of advanced aircraft configurations using new technologies include the hybrid-wing body (HWB) aircraft (see Thomas et al. [3] and Czech et al. [4]), the advanced model for extreme lift and improved aeroacoustics (AMELIA) (see Horne et al. [5]), and future supersonic aircraft (see Welge et al. [6,7] and Morgenstern et al. [8]). These latter aircraft have low-bypass ratio engines that are similar to single stream jets and are discussed by Sokhey and Kube-McDowell [9]. All of these concepts demonstrate situations where the unsteady aerodynamic noise source and resultant acoustic propagation are difficult to predict with current methodology.

Unfortunately, contemporary jet noise prediction models are incapable of predicting the noise from full-scale jet engine exhaust, let alone are capable of predicting noise when airframe surfaces are present. Two recent promising prediction approaches for installed jets include large eddy simulation (LES) by Paliath and Premasuthan [10] or Bogey [11] and a wave-packet scattering approach by Papamoschou and Mayoral [12]. The LES predictions of Paliath and Premasuthan [10] are very accurate but come at an extremely high computational cost. A direct numerical simulation (DNS) of a jet, by Freund [13] for example, is even more costly for high Reynolds numbers. Wave-packet approaches, such as those by Papamoschou and Mayoral [12], are considerably faster than LES but likely require calibration with measurement data for each jet operating condition. New jet noise prediction methods, that are fast and more first principles oriented, need to be created to address new aircraft configurations and advanced nozzle designs. In this paper, one such method is proposed that is based on the acoustic analogy of Miller [14], steady Reynolds-averaged Navier-Stokes (RANS) solutions, and a tailored Green's function.

1.1 Jet Noise Sources and Spectra

High intensity turbulence within jet plumes causes mixing noise at all frequencies and directions. It is labeled 'mixing' in the far-field power spectral density shown in Fig. 1. The vertical axis represents Sound Pressure Level (SPL) per unit Strouhal number (St). St is based on the fully expanded jet velocity and fully expanded jet diameter. Ψ is the angle in degrees measured relative to the forward nozzle centerline axis. Turbulent mixing is the predominant source of sound at subsonic jet Mach numbers and is always the dominant source of sound in the downstream direction at supersonic jet Mach numbers. Mollo-Christensen [15], Tam et al. [16], Viswanathan [17], and others have shown that large-scale coherent turbulent structures are responsible for the highest intensity noise in the downstream direction. These structures are highly coherent over multiple jet diameters. The incoherent turbulence causes acoustic radiation in all jet directions and is responsible for the highest noise intensity in the sideline and upstream jet directions. Semi-empirical fine-scale mixing noise models pioneered by Tam [18] and Tam and Auriault [19] accurately predict the sideline and upstream mixing noise. More recent descriptions by Morris and Farassat [20] yield an equivalent explanation by using an acoustic analogy approach. *The unsteady aerodynamic source and associated jet mixing noise are the focus of this paper.* Jet noise has been reviewed by many

investigators, including Ffowcs Williams [21, 22] and Goldstein [23], and specifically for supersonic jet noise by Tam [18].

When the jet Mach number is supersonic and the nozzle is operating off-design, a shock-cell structure forms and its presence creates additional noise due to high intensity turbulence convecting through the shock waves. Acoustic waves propagate to the far-field from these interactions and combine constructively and destructively to create broadband shock-associated noise (BBSAN), shown in Fig. 1. BBSAN is observed as strong broad spectral peaks with additional lower intensity peaks at higher frequencies that may dominate mixing noise. Notable models for the prediction of BBSAN are by Harper-Bourne and Fisher [24], Tam [25], Tam [26], and Morris and Miller [27]. Acoustic waves within the jet flow propagate upstream and trigger aerodynamic instabilities that close a feed-back loop that create discrete tones called 'screech,' first observed and described by Powell [28], and are also shown in Fig. 1. For additional details on screech tones see Tam [19] and for a comprehensive review see Raman [29]. Shock-associated noise is often observed in the spectra under investigation in this study.

When the propulsion system is integrated with the airframe the noise sources are altered relative to the free jet. Sawyer [30], Al-Qutub and Budair [31], and others examined the changes in aerodynamics when the jet exhaust is far from the airframe. The turbulent statistics of the jet are affected when the jet plume is multiple nozzle diameters away from the airframe. Donaldson and Snedeker [32] and Lamont and Hunt [33] showed that the turbulent statistics and shock-cell structure of jets impinging on oblique and perpendicular surfaces are significantly affected. The unsteady aerodynamic source of sound is dependent on the turbulent statistics and jet structure. Capturing variations of the acoustic source due to changes within the jet flow-field are essential for accurate predictions of jet noise. *In this paper, we attempt to capture these changes with the use of steady RANS solutions that include the nozzle and airframe geometry.*

The far-field jet noise spectrum changes significantly when the propulsion system is integrated with the airframe. This is illustrated in Fig. 2 at an inlet angle of 50 deg. for a fully expanded Mach number $M_j = 1.29$ and total temperature ratio TTR = 1.00 off-design jet. The measured free jet prediction is shown and consists of mixing and shock-associated noise. When a large flat plate extends 20 nozzle diameters, D, downstream and is $2D$ from the nozzle centerline axis in the radial direction, the measured spectrum changes dramatically as shown by the 'jet & airframe' measurement. The observer is located on the opposite side of the flat plate. Predictions for the free jet mixing noise and BBSAN can be made with the method of Miller [14] and Morris and Miller [27], illustrated by the free jet mixing noise and free jet BBSAN prediction respectively. The jet-surface interaction noise, which occurs at low frequencies typically smaller than $St < 0.1$, can be predicted by Miller [34]. Studies of Curle [35], Ffowcs Williams and Hawkings [21], Ffowcs Williams and Hall [36], Crighton and Leppington [37], and Amiet [38], suggest that the most dominant source of interaction noise is generated by the turbulence within the shear layer of the jet convecting downstream past the trailing edge of the wing or airframe. The jet-surface interaction noise is a combination of unsteady loading on the airframe surface within the boundary layer (see Curle [35]) and an interaction and subsequent diffraction of the jet turbulent flow about the trailing edge (see Ffowcs Williams and Hall [36]). Note that at this particular angle and jet condition, the sound intensity is a combination of jet-surface interaction noise, mixing noise, and BBSAN. *The main focus of this paper is the prediction of mixing noise scattered by the airframe.*
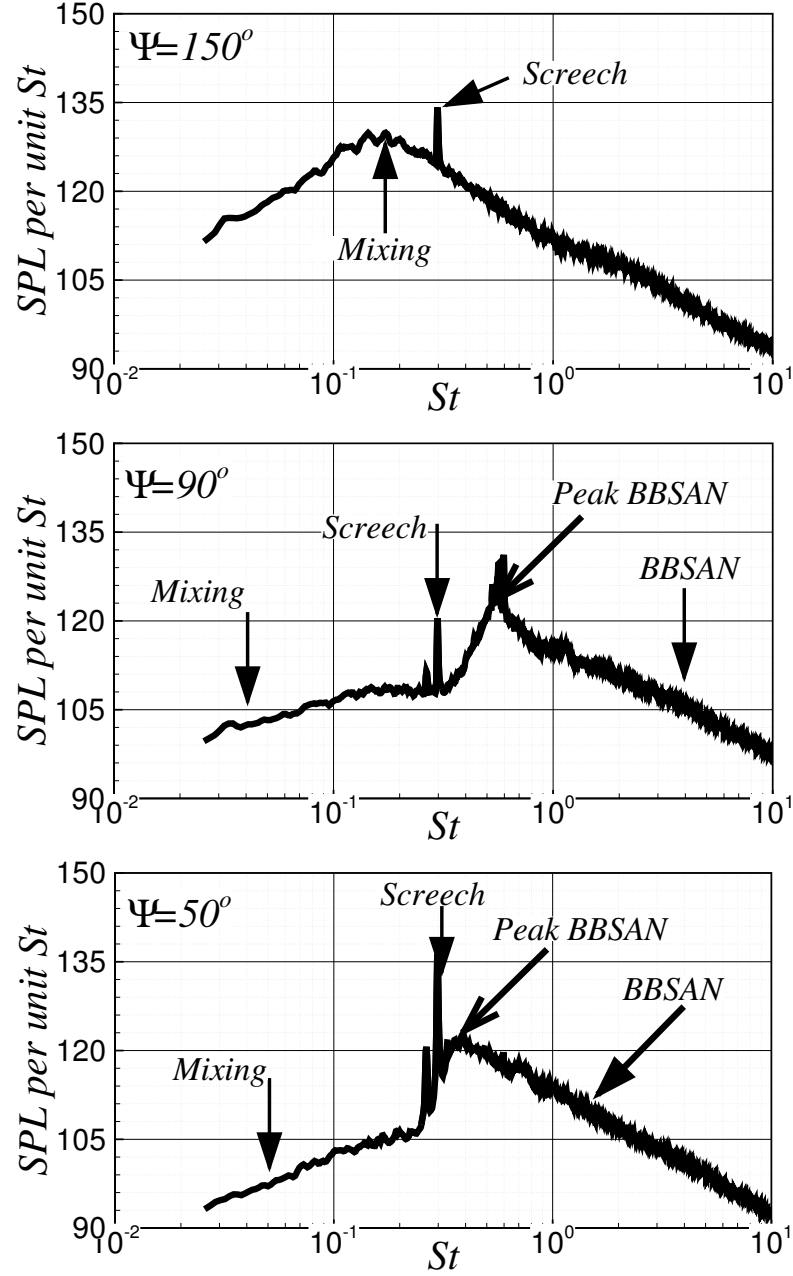
4

Figure 1. Sound pressure level per unit St resulting from an off-design heated supersonic jet. Ψ is the angle from the upstream jet axis to the observer centered about the nozzle exit. The observers are located 100 nozzle exit diameters from the center of the nozzle exit.
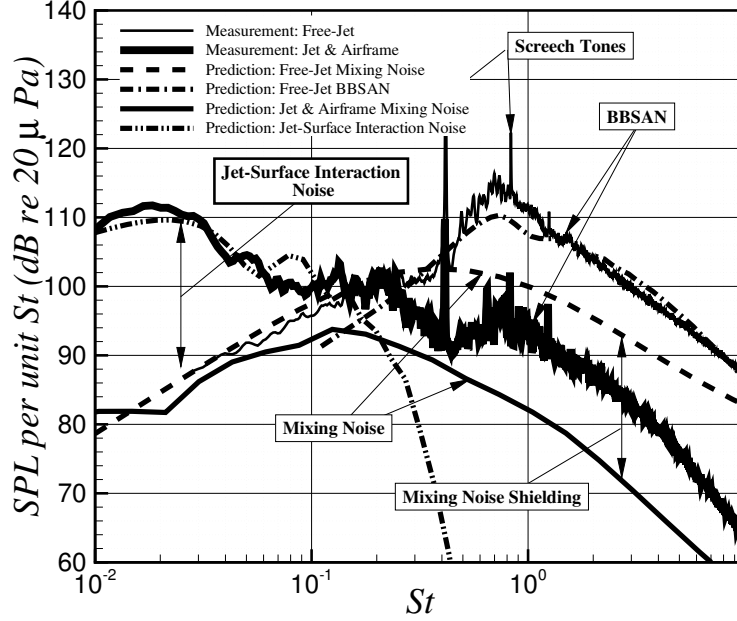
Figure 2. The free jet and installed jet predictions at $R/D = 100$ and $\Psi = 50$ deg. compared with measurement. The jet operates at $M_j = 1.29$ and TTR = 1.00 from the SMC016 nozzle with $D = 0.0508$ m and the plate is located at $x_p/D = 20$ and $y_p/D = -2$.

1.2 The Prediction of Jet Mixing Noise

Many methods have been developed to predict jet mixing noise. Lighthill [39, 40] pioneered the acoustic analogy approach, which is an exact rearrangement of the equations of motion into a wave operator and inhomogeneous equivalent source term. Lilley [41] created an acoustic analogy that included refraction effects in the propagation operator allowing for realistic shear layer refraction effects to be accounted for. Khavaran [42] developed a prediction method that followed the 'MGB' code of Mani et al. [43] but differed significantly by informing the equivalent sources with a steady RANS solution. The approach of Khavaran [42] has the benefit of including the nozzle geometry in the calculation and shock waves within the jet plume. An alternative approach to the acoustic analogy was created by Tam and Auriault [19] who developed a semi-empirical theory for fine-scale mixing noise based on observations of Tam et al. [16]. Morris and Farassat [20] and later Morris and Boluriaan [44] examined the model of Tam and Auriault [19] and formulated a similar source in terms of an acoustic analogy. Recently, Miller [14] used the model basis of Morris and Farassat [20] and Tam and Auriault [19] and predicted single and dual stream jet noise for a wide range of jet Mach numbers and temperature ratios. *This latter theory is modified for predictions of jet mixing noise about the flight vehicle airframe.* These predictions are shown in Fig. 2 as lines labeled 'Mixing Noise' and require knowledge of how sound is scattered by the flight vehicle airframe.

1.3 The Scattering of Sound from Flight Vehicles

Separate techniques have been developed to predict the scattering of noise from jets about flight vehicle airframes. They are typically based on the solution of the Helmholtz or convective wave equation. One popular approach uses the boundary element method (BEM) that solves an integral equation for the Helmholtz equation. It was recently applied successfully by Huang and

Papamoschou [45]. It has also been applied by Agarwal and Dowling [46] to predict monopole acoustic shielding of a blended wing body aircraft. Solving the linear system associated with the BEM approach can become computationally expensive because the order of the matrix depends on the size of the aircraft and the need to meet the Nyquist criteria.

The equivalent source method (ESM) follows the same approach as the BEM which replaces the boundary value problem (BVP) with a distribution of multipoles located inside the scattering body. An excellent overview is given by Dunn [47] and applied in NASA's Fast Scattering Code (FSC) by Tinetti et al. [48]. The fundamental advantage of the ESM over other boundary methods is that the resulting linear system of equations can be considerably smaller than those arising from the BEM. We use predictions of FSC [49] to help validate the approach adopted in this paper.

Another approach for acoustic scattering is based on the geometric theory of diffraction (acoustic ray theory). This approach offers several advantages. For example, the method's computational cost is frequency independent and rays need to only be traced once for all frequencies of interest (see Agarwal et al. [50] for details). Also, it is not computationally dependent on the geometry size but only the complexity. These are key advantages relative to other methods, which have great computational costs for high frequencies and large geometries. Unfortunately, there are a limited number of source models for scattering. In this work, *we will connect a custom ray tracing solver (that provides a tailored Green's function) with the acoustic analogy of* Miller [14].

1.4 *ab initio ad finem*

The remainder of this paper is organized as follows. A mathematical model is reviewed that is based on the acoustic analogy of Miller [14, 51]. The calculation of the vector Green's function within the acoustic analogy is described using the geometric theory of diffraction. To quantify the propulsion airframe aeroacoustic installation effects on the aerodynamic noise source, a non-dimensional number, Γ, is proposed that is dependent on the jet operating conditions and airframe location. Steady RANS solutions of free and installed jets are compared with particle image velocimetry (PIV) measurements of Bridges and Wernet [52]. The non-dimensional number, Γ, is evaluated and compared with noise predictions using the validated steady RANS solutions. The ray tracing approach is validated with measurements by Ahtye and McCulley [53] of a point source near a flat plate. Ray tracing is then used in conjunction with an acoustic analogy to predict far-field mixing noise generated from a jet shielded by a flat plate. These predictions are validated with measurements of Brown et al. [54]. Finally, a summary and conclusion are presented.

2 Mathematical Analysis

2.1 An Acoustic Analogy Approach

An acoustic analogy is an arrangement of the governing equations of motion into an operator that supports wave propagation and is equated to equivalent sources. The acoustic analogy of Miller [14, 51] is based on the analogy of Morris and Farassat [20] and is used as the basis of this prediction approach. Following their approach, the Euler equations are arranged into the inhomogeneous LEE in which the acoustic propagation and equivalent sources are separated. A convolution integral of the vector Green's function of the LEE and the equivalent sources define the fluctuating pressure in the far-field. Using an approximation by Tam and Auriault [19], two closely placed source points in the jet are related, and the spectral density is written in terms of the two-point cross-correlation of the equivalent sources and the vector Green's function of the LEE. The spectral density, S, of the far-field fluctuating acoustic pressure is,

$$S(\boldsymbol{x}, \omega) = \rho_\infty^2 c_\infty^4 \int_{-\infty}^{\infty} \int_{-\infty}^{\infty} \int_{-\infty}^{\infty} \frac{2\pi^{3/2} c_\infty^2 l_x l_y l_z \tau_s x^2}{c_\infty^2 x^2 + (ux_1 + vx_2 + wx_3 + c_\infty x)^2 \tau_s^2 \omega^2}$$

$$\times \left\{ \pi_g^{*0}(\boldsymbol{x}, \boldsymbol{y}, \omega) \pi_g^0(\boldsymbol{x}, \boldsymbol{y}, \omega) A_s^2 \frac{(u_s/c_\infty)^4}{\tau_s^2} + \sum_{n=1}^{3} \sum_{m=1}^{3} \pi_g^{*n}(\boldsymbol{x}, \boldsymbol{y}, \omega) \pi_g^m(\boldsymbol{x}, \boldsymbol{y}, \omega) B_s^2 \frac{(u_s/c_\infty)^2 u_s^4}{l_x^2} \right\} \quad (1)$$

$$\times \exp\left[-\frac{\left(l_x^2 x_1^2 + l_y^2 x_2^2 + l_z^2 x_3^2\right) \omega^2}{4 c_\infty^2 x^2} \right] d\boldsymbol{y},$$

where π_g^n is the nth component of the vector Green's function of the LEE. The other variables are defined in the nomenclature.

Details regarding the development of Eqn. 1 are discussed in Miller [14]. The scales of turbulence in Eqn. 1, l_x, l_y, l_z, u_s, and τ_s, are required to conduct a prediction. These can be found by simple empirical models or unsteady CFD simulations. Here, they are related to a steady RANS solution by, $l_x = c_l K^{3/2}/\epsilon$, $\tau_s = c_\tau K/\epsilon$, and $u_s = c_u (2K/3)^{1/2}$.

The coefficients are $c_\tau = 0.30$, $c_u = 1.00$, and $c_l = 1.00$. These coefficients are based on a reference jet operating at the sonic condition, TTR = 3.20, and a 0.0508 m convergent nozzle at the sideline location of $R/D = 100$. They have been calibrated by the same methodology of Tam and Auriault [19]. Their variation from Tam and Auriault is attributed to the use of a different acoustic analogy and steady RANS solver. The cross-stream turbulent length scales, l_y and l_z, are set to 3/10 of l_x, which corresponds to experimental observation. Coefficients associated with the turbulent length scales are never altered irrespective of the jet Mach number, temperature, nozzle geometry, or any other parameter.

A solution for π_g^n is now required. One method suitable for calculating the vector Green's function of the LEE is by finding the Green's function of Lilley's [41] equation. For a parallel axisymmetric mean flow the Green's function of the LEE can be written in terms of the Green's function of Lilley's equation. Morris and Boluriaan [44] show that the vector Green's function of the LEE is related to the Green's function of Lilley's [41] equation by,

$$\pi_g^0(\boldsymbol{x}, \boldsymbol{y}, \omega) = \omega^2 g_l(\boldsymbol{x}, \boldsymbol{y}, \omega) - 2i\overline{u}\omega \frac{\partial g_l(\boldsymbol{x}, \boldsymbol{y}, \omega)}{\partial y_x} - \overline{u}^2 \frac{\partial^2 g_l(\boldsymbol{x}, \boldsymbol{y}, \omega)}{\partial y_x^2}, \quad (2)$$

$$\pi_g^1(\boldsymbol{x}, \boldsymbol{y}, \omega) = -\left(i\omega + \overline{u}\frac{\partial}{\partial y_x}\right) \frac{\partial}{\partial y_x} g_l(\boldsymbol{x}, \boldsymbol{y}, \omega), \quad (3)$$

$$\pi_g^2(\boldsymbol{x}, \boldsymbol{y}, \omega) = -\left\{ 3\frac{\partial \overline{u}}{\partial y_r}\frac{\partial}{\partial y_x} - \left(i\omega + \overline{u}\frac{\partial}{\partial y_x}\right)\frac{\partial}{\partial y_r} \right\} g_l(\boldsymbol{x}, \boldsymbol{y}, \omega), \quad (4)$$

$$\pi_g^3(\boldsymbol{x}, \boldsymbol{y}, \omega) = -\left(i\omega + \overline{u}\frac{\partial}{\partial y_x}\right) \frac{1}{y_r}\frac{\partial}{\partial y_\theta} g_l(\boldsymbol{x}, \boldsymbol{y}, \omega), \quad (5)$$

where the subscript of the source vector $\boldsymbol{y}$ denotes the direction in which the partial derivative is taken. The problem is now reduced to finding the Green's function of Lilley's [41] equation instead of the full vector Green's function of the LEE. Morris and Miller [55] used a similar technique and found an analytic solution of the vector Green's function of the LEE related to the Green's function of the Helmholtz equation for quiescent flow (see Eqn. 23 of Morris and Miller). Tam and Auriault [56] and Raizada [57] also used this technique with success. These methods use an adjoint approach and are relatively computationally inexpensive. However, these methods do not include

a scattering surface such as the airframe or ground, thus analytic or numerical approximations of Lilley's equation that have the potential to include a scattering surface are sought.

An asymptotic solution of Lilley's equation for low frequencies was found by Goldstein [58–60] and for high frequencies by Balsa et al. [61]. Miller [51] examined the asymptotic solutions of Lilley's equation, the Green's function of the convective Helmholtz equation, g, and a matching function, and proposed,

$$g_l(\boldsymbol{x}, \boldsymbol{y}, \omega) \approx \frac{i}{c_\infty^2 c_0^{c_\alpha} \omega} \frac{c_\infty}{\bar{c}} \exp\left[\frac{-i\omega}{c_\infty} \left\{x \cos\theta + r \sin\theta \cos\left(\phi_0 - \phi\right)\right\}\right] q_e g, \tag{6}$$

where $\bar{c}$ is the local speed of sound, $c_\beta = 1 \times 10^{-4}$, $q_e = \exp\left[-c_\beta \omega / c_\infty\right]$ for $Re[g_o^*] \leq 0$, c_0 is Ribner's convection coefficient, c_α is the amplification power coefficient and is otherwise unity, and the remaining terms are described in Miller [51].

The benefit of this approach is existing numerical solvers can provide the Green's function of the convective Helmholtz equation. For example, the Fast Scattering Code (FSC) by Tinetti and Dunn [49], any BEM (see an overview by Katsikadelis [62]), or FastBEM by Liu [63]. This provides the ability to predict jet noise scattering from any surface as long as the noise sources are minimally affected by the airframe. Here, we find a tailored form of g using the geometric theory of diffraction described in the next section.

2.2 A Tailored Green's Function

The propagation of sound about the flight vehicle airframe is governed by g. Here, a ray tracing approach is used to provide the tailored Green's function. For free jet predictions the free-field Green's function of the Helmholtz equation is used,

$$g = \frac{\exp[ikr]}{4\pi r}, \tag{7}$$

where $\boldsymbol{r} = \boldsymbol{x} - \boldsymbol{y}$ is a vector from the source to observer. When a scattering geometry such as the airframe is integrated with the jet, the tailored Green's function of the Helmholtz equation is found using a ray tracing approach. In this case, the tailored Green's function is the sum of contributions from the incident and diffracted field,

$$g = g_I + \sum g_D, \tag{8}$$

where g_I is the incident ray, equivalent to the free-field Green's function in Eq. 7, and g_D are the diffracted rays. The diffracted rays consist of edge and corner diffracted rays.

2.3 The Geometric Theory of Acoustic Rays

In this section, an overview of the ray tracing method is presented that is used to evaluate Eqn. 8. A shadow region exists where there is no direct line of sight from source to observer. The theory, developed by Keller [64], has been recently used in the area of propulsion airframe aeroacoustics to aid in the study of shielding effects (see Suzuki [65], Agarwal [50], van Rens [66], and Lummer [67] for example). Kinsler et al. [68] showed that under certain circumstances energy on defined paths can be approximated as rays rather than waves.

We assume a solution for the convective Helmholtz equation of the form, $\hat{p}(\boldsymbol{x}) = A(\boldsymbol{x}, \omega) \exp[i\omega\tau(\boldsymbol{x})]$, where $\hat{p}(\boldsymbol{x})$ is the Fourier transform of the complex pressure, $\tau(\boldsymbol{x}) = T(\boldsymbol{x})/c_\infty$ is the quantity known as the eikonal (see Kinsler et al. [68] for details), and ω is the radial frequency. Constant values of $T(x)$ define surfaces of constant phase. Substitution of the assumed solution into the governing

equation and equating the real and imaginary parts of the resulting equation yields two equations that are coupled and nonlinear. The high frequency limit allows for a simple solution to be obtained. It is assumed that an asymptotic expansion of the pressure amplitude, $A(x, \omega)$, exists as a power series (see Pierce [69] for details) in inverse powers of radial frequency,

$$A(\boldsymbol{x}, \omega) = \sum_{n=0}^{\infty} \frac{A_n(\boldsymbol{x})}{\omega^n}. \tag{9}$$

By using Eqn. 9 and eliminating all terms except those with the two highest orders of magnitude of ω, a simplified equation is obtained, $i\omega \left(2\nabla\tau\nabla A_0 + \nabla^2\tau A_0 \right) - \omega^2 A_0 \left[(\nabla\tau)^2 - c^{-2} \right] = 0$. It is assumed that A_0 is an approximation of A for large radial frequencies, $\lim_{\omega \to \infty} A(\boldsymbol{x}, \omega) = A(\boldsymbol{x})$. Separation of the real and imaginary terms and further simplification result in,

$$(\nabla\tau)^2 = \frac{1}{c^2} \qquad or \qquad (\nabla T)^2 = \frac{c_\infty^2}{c^2} = n^2 \tag{10a}$$

$$2\nabla\tau\nabla A + \nabla^2\tau A = 0 \qquad or \qquad \nabla \cdot \left(A^2\nabla\tau \right) = 0. \tag{10b}$$

Equation 10a is the eikonal equation where $n = c^{-1}c_\infty$ is the index of refraction. The second part of Eqn. 10a is formed from multiplying by A and using $\nabla \cdot (\phi\vec{B}) = \phi\nabla \cdot \vec{B} + \nabla\vec{B} \cdot \phi$. It can be shown from Eqn. 10a that (see Kinsler [68] for details), $\nabla T = n\hat{s}$, where $\hat{s}$ is the unit vector that gives the local direction of propagation. To determine how the amplitude A varies along a ray, Eqn. 10b is solved using ray tube areas (see Pierce [69] for details). Rays travel in the direction $\nabla T = \hat{s}$ and only pass through the end caps of volume elements, thus the integral over the surface of the side of the ray tube vanishes. Using these assumptions we obtain,

$$A^2(\boldsymbol{x})S(\boldsymbol{x})(\nabla\tau \cdot \vec{\boldsymbol{n}})_{\boldsymbol{x}} - A^2(\boldsymbol{x}_0)S(\boldsymbol{x}_0)(\nabla\tau \cdot \vec{\boldsymbol{n}})_{\boldsymbol{x}_0} = 0, \tag{11}$$

where $\vec{\boldsymbol{n}}$ is the surface normal vector. If the ray is passing through a homogeneous medium ($c = $ constant), then $(\hat{s} \cdot \vec{\boldsymbol{n}})_{\boldsymbol{x}} = (\hat{s} \cdot \vec{\boldsymbol{n}})_{\boldsymbol{x}_0}$ and the pressure amplitude at $\boldsymbol{x}$ along the ray tube is, $A(\boldsymbol{x}) = A(\boldsymbol{x}_0) \left[S(\boldsymbol{x}_0)/S(\boldsymbol{x}) \right]^{1/2}$. Energy within a ray tube (SA^2) remains constant within the limitation set forth by the eikonal equation. Incident rays that impinge on surface edges, corners, or slightly graze the surface create diffracted rays that propagate to the shadow region. There are multiple rays that account for the diffracted field; edge diffracted rays, creeping rays, and corner diffracted rays.

2.3.1 Edge Diffracted Rays

Edge diffracted rays are based on a modified form of Fermat's principle. Fermat's principle states that an edge diffracted ray from $\boldsymbol{S}$ to $\boldsymbol{O}$ is a curve that has stationary optical length among all curves from $\boldsymbol{S}$ to $\boldsymbol{O}$ with one point on the edge (see Keller [64]). The curves correspond to paths that can be traversed in the least time. Sommerfeld [70] showed that waves diffracting by a semi-infinite edge diffract in a direction normal to the edge in the form of a cylindrical wave. Fermat's principle for edge diffraction implies that the diffracted and incident ray have corresponding angles relative to the point of diffraction, as long as they share the same medium. These principles of diffracted rays are illustrated in Fig. 3.

After the ray is diffracted, it has similar properties to the incident ray, but is dependent on the point of diffraction. The acoustic pressure field at the diffraction point on the edge is determined using the solution, $\hat{p}(\boldsymbol{V}) = A(\boldsymbol{S}, \omega) |\boldsymbol{V} - \boldsymbol{S}|^{-1} \exp[i\omega\tau]$, where $\boldsymbol{S}$ is the source location and $\boldsymbol{V}$ is

the diffraction location on the edge. The acoustic pressure field at the diffraction point determines the initial amplitude and phase of the diffracted ray. The phase of the diffracted ray is the eikonal added to the phase at the diffraction point. The amplitude of the diffracted ray is governed by the ray tube area relationship. Therefore, the energy per unit area of the diffracted ray tube is proportional to r^{-1} and the amplitude is proportional to $r^{-1/2}$. Assuming that the amplitude of the diffracted ray is proportional to the amplitude at the point of diffraction, the acoustic pressure of the diffracted ray is,

$$\hat{p}(\boldsymbol{O}) = D\hat{p}(\boldsymbol{V}) \left[\frac{\rho}{r(r + \rho)} \right]^{1/2} \exp[i\omega\tau], \tag{12}$$

where D is the diffraction coefficient, r is the distance from the edge to observer, $|\boldsymbol{O} - \boldsymbol{E}|$, and ρ is the distance from source to observer $|\boldsymbol{O} - \boldsymbol{S}|$. Keller [64] showed that Eqn. 12 satisfies Sommerfeld's [70] exact solution for diffraction of a wave by a half-plane when it is asymptotically expanded for large frequencies. The resultant diffraction coefficient is,

$$D = \frac{\sin(\pi/n)\exp[i\pi/4]}{n(2\pi k)^{1/2}\sin(\theta)} \left[\frac{1}{\cos\frac{\pi}{n} - \cos\frac{\phi_s - \phi_o}{n}} + \frac{1}{\cos\frac{\pi}{n} - \cos\frac{\phi_s + \phi_o + \pi}{n}} \right], \tag{13}$$

where $k = 2\pi f/c_\infty$ is the wave number, ϕ_s is the polar angle to the incident ray, ϕ_o is the polar angle to the diffracted ray, and θ is the oblique angle between the edge and incident ray. Here, n is a parameter of the wedge angle, $\beta = n\pi$, where β is the angle of the wedge. The angles are illustrated in Figs. 3 and 4. Analysis of a half-plane corresponds to $n = 2$. Adopting a simplification from Agarwal et al. [50], a wedge index $\nu = \pi/\beta$ is used to redefine the diffraction coefficient as,

$$D = \frac{\nu \sin(\nu\pi)\exp[i\pi/4]}{(2\pi k)^{1/2}\sin(\theta)} \left[\frac{1}{\cos(\nu\pi) - \cos(\nu(\phi_s - \phi_o))} + \frac{1}{\cos(\nu\pi) - \cos(\nu(\phi_s + \phi_o + \pi))} \right]. \tag{14}$$

The contribution to the acoustic field from a single diffracted ray can be calculated using Eqns. 12 and 14 and the variables illustrated in Figs. 3 and 4.
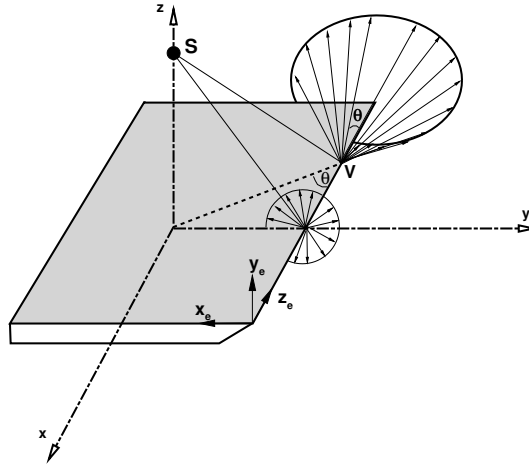

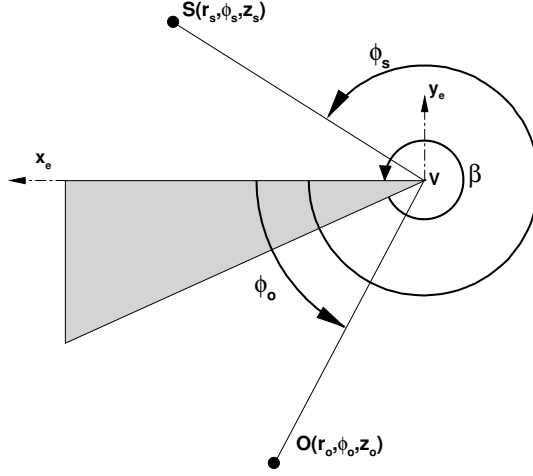Figure 3.   Edge diffraction and associated variables.

Figure 4. Variables associated with diffraction on a sharp edge.

2.3.2 Creeping Rays

Creeping rays, also known as surface diffracted rays, are produced when a ray is incident tangentially to a smooth boundary or interface (see Levy and Keller [71] for details). After the incident ray grazes the surface tangentially, it travels along the surface and continuously sheds a diffracted ray, as shown in Fig. 5. The diffracted rays are continuously emitted at angles tangent to the surface. Creeping rays are based upon an alternate form of Fermat's principle, that a surface diffracted ray from a point S to a point O is a curve that makes stationary the optical length among all curves from S to O having an arc on the boundary. This implies that S to S_T and O_T to O are straight lines tangent to the surface at S_T and O_T respectively, and S_T to O_T is a geodesic curve on the surface (see Fig. 4).
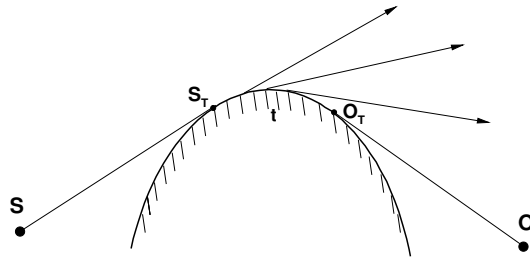
Figure 5. Incident ray diffracting from a smooth surface.

A solution for a surface diffracted ray, similar to the edge diffracted ray, is proposed by Levy and Keller [71],

$$\hat{p}(\boldsymbol{O}) = T(\boldsymbol{S}_T, \boldsymbol{O}_T)\hat{p}(\boldsymbol{S}_T) \left[\frac{\rho}{r(r+\rho)}\right]^{1/2} \exp[i\omega\tau], \tag{15}$$

where $T(\boldsymbol{S}_T, \boldsymbol{O}_T)$ is a transfer function that relates the diffracted field at the two tangent points $\boldsymbol{S}_T$ and $\boldsymbol{O}_T$ (see Agarwal et al. [72]). The function $T(\boldsymbol{S}_T, \boldsymbol{O}_T)$ is given by,

$$T(\boldsymbol{S}_T, \boldsymbol{O}_T) = \sum_m D_m(\boldsymbol{S}_T) D_m(\boldsymbol{O}_T) \exp\left[ikt - \int_0^t \alpha_m(\tau) d\tau \right] \left(\frac{d\sigma(\boldsymbol{S}_T)}{d\sigma(\boldsymbol{O}_T)} \right)^{1/2}, \tag{16}$$

where $D_m(\boldsymbol{S}_T)$ is the diffraction coefficient at $\boldsymbol{S}_T$, α_m is the decay coefficient, t is the distance along the curve, and $[d\sigma(\boldsymbol{S}_T)/d\sigma(\boldsymbol{O}_T)]^{1/2}$ is the attenuation of the ray field due to the divergence of two nearby creeping rays. These values are problem specific and are based on the diffraction geometry, material properties, and acoustic wave number. These values have been evaluated for simple problems such as a cylinder and a sphere by Levy [71]. Equation 16 shows that the creeping ray exponentially decreases with the distance along the path. If $t << r$, where r is the distance to the observer, the creeping ray converges to the solution of an edge diffracted ray. If $t >> r$, the amplitude of the ray decreases exponentially and has a negligible contribution to the diffracted field relative to an edge diffracted ray.

2.3.3 Corner Diffracted Rays

Incident rays that impinge on a sharp corner of the airframe are diffracted as spherical waves as described by Keller [73]. The cross-sectional area of the corner diffracted ray tube is proportional to r^{-2} and the amplitude is proportional to r^{-1}. Following the same derivations for edge diffracted rays, the complex acoustic pressure of the corner diffracted ray is,

$$\hat{p}(\boldsymbol{O}) = \frac{C\hat{p}(\boldsymbol{V})}{|\boldsymbol{O} - \boldsymbol{V}|} \exp[i\omega\tau], \tag{17}$$

where C is the corner diffraction coefficient. The coefficient C is analogous to D and depends on the geometry, direction of the incident and diffracted ray, and wavenumber. C is proportional to k^{-1} and the corner diffracted field decreases faster than the edge diffracted field as k increases. Many forms of C exist and due to their multitude and complex nature they are not surveyed here (see Kraus [74], Felsen [75], and Siegel [76] for details).

2.4 A Non-Dimensional Theory

We now turn our attention to the development of a non-dimensional number to quantify the effect that the airframe has on the jet mixing noise source. Parameters are identified that alter the noise source with varying jet operating condition and airframe position relative to the nozzle exit. The first parameter is the fully expanded diameter of the jet which represents the equivalent nozzle exit diameter for a shock free flow,

$$D_j = D \left(\frac{1 + \frac{\gamma-1}{2}M_j^2}{1 + \frac{\gamma-1}{2}M_d^2} \right)^{(\gamma+1)/4(\gamma-1)} \left(\frac{M_d}{M_j} \right)^{1/2}, \tag{18}$$

where D is the nozzle exit diameter and γ is the ratio of specific heats.

Additionally, x_p is the distance from the nozzle exit to the trailing edge of the airframe[1] parallel to the jet centerline. y_p is the characteristic length from the nozzle centerline to the nearest airframe surface. x_I is the axial distance from the nozzle exit to the jet impingement location, is a function of the jet spreading rate, and is approximated as,

---

[1]We elect to use the terms 'airframe' and 'flat plate' interchangeably in terms of this analysis.

$$x_I = \frac{y_p - D/2}{\tan[\delta_\eta]}, \tag{19}$$

where δ_η is the spreading angle of the jet. Values of δ_η are not readily available without numerical calculations or measurement. An empirical model developed by Lau [77] is adopted for δ_η,

$$\delta_\eta = 0.177 \left(1 - 0.294 M_j^2\right) \left(1 + \frac{1}{2}(M_j^2 - 1)(T_j/T_o - 1.4)^2\right), \tag{20}$$

which is valid for a wide range of single-stream jet Mach numbers and temperature ratios. The flows of this investigation fall within the range of validity of Eqn. 20. Using these variables a non-dimensional number is proposed,

$$\Gamma = \left(\frac{D_j}{y_p}\right)\left(\frac{x_p}{x_I}\right). \tag{21}$$

Using the approximation of x_I from Eqn. 19, Eqn. 21 is written as,

$$\Gamma = \frac{D_j x_p \tan[\delta_\eta]}{y_p(y_p - D/2)}, \tag{22}$$

where $y_p > D/2$. Physically, Eqn. 22 is the ratio of the product of jet and airframe length scales divided by the cross-stream length scale and interaction distance. Small values of Γ imply that airframe effects on the jet aerodynamic noise sources are negligible. Likewise, large values of Γ imply that the effects of the airframe on the aerodynamic noise sources of the jet are very large. Equation 22 is evaluated in the next section using different jet conditions and airframe surface positions, and compared with numerical predictions for the variation of noise from the aerodynamic source.

3   Application

3.1   Application of the Acoustic Analogy

Equation 1 is implemented in a computer program. The program uses structured or unstructured steady RANS solutions and converts the specific dissipation, Ω, to dissipation $\epsilon = 0.09K\Omega$. The steady RANS solution is interpolated using the inverse weighted distance method onto a new structured grid that encompasses the jet plume. Numerical integration is performed using the new structured domain to approximate the integrals of the model equations. Interpolated values reside on the x-y plane and are subsequently rotated about the jet centerline axis to form a cylindrical region encompassing the plume. Integration ranges and grid point density are varied until the solution is grid independent. The streamwise integration range extends from $10^{-4}D \leq x \leq 20D$ and in the radial direction from $10^{-4}D \leq r \leq 2D$. The structured domain contains 300 grid points in the streamwise direction and 100 grid points in the radial direction. The angle between each plane in the azimuthal direction is 15 degrees. Doubling the number of grid points in the streamwise or radial direction or doubling the number of azimuthal planes, relative to the converged solution, has negligible effect on the solution.

Equation 1 is evaluated by approximating the integrals as summations. At each grid point the local volume is multiplied by the integrand and the pre-factor. The integrand contains arguments that are obtained from the steady RANS solutions. Evaluation of Eqn. 1 also requires a tailored Green's function that is unique from each source point, $\boldsymbol{y}$, to each observer, $\boldsymbol{x}$ on a radial frequency

14

basis. The integrand of Eqn. 1 contains the vector Green's function of the LEE shown in Eqns. 2 through 5. Equations 2 through 5 are dependent on a steady RANS solution and the Green's function of Lilley's equation, g_l. Here, g_l is written in terms of the Green's function of the convective wave equation. In the absence of a scattering surface such an aircraft airframe, g is calculated using Eqn. 7. When a scattering surface is present, Eqn. 8 is used, where the arguments depend on the incident or diffracted ray path. Here, the developed ray theory is used to find g for each source point and frequency. This is performed within the computer program by calling subroutines that are described in the next section.

3.2 Application of the Ray Theory

The developed ray theory is implemented in the same computer program as the acoustic analogy. Some specific computational strategies are used to evaluate the developed ray theory and are described here. The implementation is summarized as follows: read the scattering geometry, find the three-dimensional projection of the geometry, find the edge of the geometry, test if the observer is in the shadow zone, find all diffracted rays associated with an observer, and sum the existing diffracted and incident rays in the complex field. The geometry of the airframe is read into the memory of the computer and includes the source and observer locations. Next, the three-dimensional projection of the scattering object based on the calculated ray paths is found. This projection is created via a 'rotation matrix' and is used to temporarily rotate the airframe to a new reference frame. The rotation is performed by creating a z-axis ($\boldsymbol{z}'$) based on the vector between the observer and the source location. If $\boldsymbol{O} = [O_1, O_2, O_3]$ is the observer location and $\boldsymbol{S} = [S_1, S_2, S_3]$ is the source location then, $\boldsymbol{z}' = \boldsymbol{S} - \boldsymbol{O}/|\boldsymbol{S} - \boldsymbol{O}|$. Corresponding $\boldsymbol{x}'$ and $\boldsymbol{y}'$ axes are arbitrary, orthonormal, and follow a right-hand rule convention. Here, we adopt the following rule of orthogonality, $\boldsymbol{z}' \cdot \boldsymbol{x}' = 0$. We form a simple solution, $\boldsymbol{x}' = [z_2', -z_1', 0]$ and $\boldsymbol{y}' = \boldsymbol{z}' \times \boldsymbol{x}'$.

Using the new axes, a rotation matrix is formed and multiplied by the node locations of the airframe geometry to determine the projected coordinates in the $\boldsymbol{x}' - \boldsymbol{y}'$ plane,

$$\begin{bmatrix} x_{proj} \\ y_{proj} \end{bmatrix} = \begin{bmatrix} x_1' & x_2' & x_3' \\ y_1' & y_2' & y_3' \end{bmatrix} \begin{bmatrix} x \\ y \\ z \end{bmatrix}. \tag{23}$$

The edge, or diffraction outline, of the airframe geometry is now determined based on the source and observer location. Edges that are unique to elements are on the boundary in the projected domain and are only specified once to describe an element. For example, if two elements share an edge then that edge is not unique and not on the boundary of the geometry for a particular source and observer. An example is shown in Fig. 6 that illustrates the edge in the projected plane for a discretized sphere.

An approach by Glassner [78] is modified to test if the observer is within the shadow region relative to the source. This approach solves two equations. One equation describes the ray path and the second the airframe. If a real solution exists then there is an intersection of the ray and airframe geometry, thus the observer is in the shadow zone. Here, we modify the approach of Glassner and use the edge determined in the projected plane, as previously described, which is based upon two-dimensional polygons. The point of intersection is determined by using the equation for the three-dimensional projected plane. It can then be determined if the intersection point is within the boundaries of the edge on the two-dimensional plane. Figure 7 illustrates this process for a ray intersecting a spherical object. A new reference frame, $\hat{u} - \hat{v}$, is established with the origin at the point of intersection on the two-dimensional plane. Each edge segment is examined for intersection
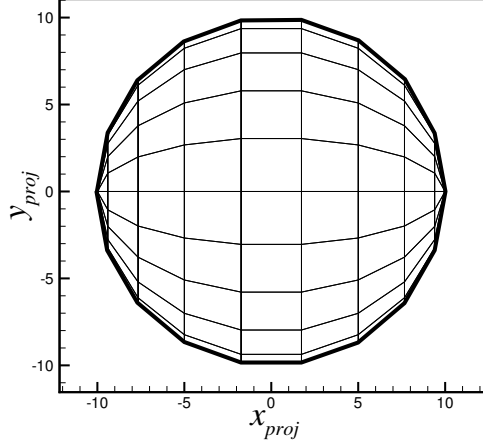
Figure 6. The unique edges from the projected plane.

relative to the positive $\hat{u}$-axis. If only one edge segment intersects the positive $\hat{u}$-axis then the point is within the two-dimensional boundary. If there are zero or two edge segments crossing the positive $\hat{u}$-axis, the point is outside the two-dimensional boundary. An example is shown in Fig. 7, where the first intersection point crosses the positive $\hat{u}$-axis and the second intersection point has zero edge segments crossing the positive $\hat{u}$-axis.

The equation for a cone about an arbitrary axis is,

$$(\boldsymbol{O} - \boldsymbol{V})^T \, \boldsymbol{N} = (\boldsymbol{O} - \boldsymbol{V})^T \, (\boldsymbol{O} - \boldsymbol{V}) \cos \theta, \tag{24}$$

where $\boldsymbol{O}$ is the observer location on the surface of the cone, $\boldsymbol{V}$ is the point of diffraction and vertex of the cone, $\boldsymbol{N}$ is the axis of the cone and unit vector of the edge, and θ is the angle of the cone. Relevant angles of diffraction are displayed in Fig. 3. All observer points $\boldsymbol{O}$ that satisfy Eqn. 24 are on the surface of the cone and have a diffracted ray edge point $\boldsymbol{V}$. The angle θ is,

$$\theta = \cos^{-1} \left(\frac{[\boldsymbol{V} - \boldsymbol{S}] \cdot \boldsymbol{N}}{|\boldsymbol{V} - \boldsymbol{S}|} \right). \tag{25}$$

Combining Eqns. 24 and 25 yield an equation for the vertex vector location $\boldsymbol{V}$,

$$\sqrt{(V_1 - S_1)^2 + (V_2 - S_2)^2} \left\{ N_1(O_1 - V_1) + N_2(O_2 - V_2) + N_3(O_3 - V_3) \right\}$$
$$= \left\{ (V_1 - S_1)^2 + (V_2 - S_2)^2 + (V_3 - S_3)^2 \right\} \left\{ N_1(V_1 - S_1) + N_2(V_2 - S_2) \right\}. \tag{26}$$

Equation 26 is parameterized by t on a straight edge segment. The parameterized equations are,

$$V_i = E_i^0 + (E_i^F - E_i^0)t, \tag{27}$$

where $\boldsymbol{E}^0$ and $\boldsymbol{E}^F$ are the first and second end point of the edge segment respectively and t is the proportionate distance along the edge segment. Figure 3 shows these quantities and the cone parameters. Using the parameters in Eqns. 26 and 27, t is found in the region $0 \le t \le 1$ using the secant method. If a real solution for t exists for $0 \le t \le 1$, the diffraction point, source location, and

16
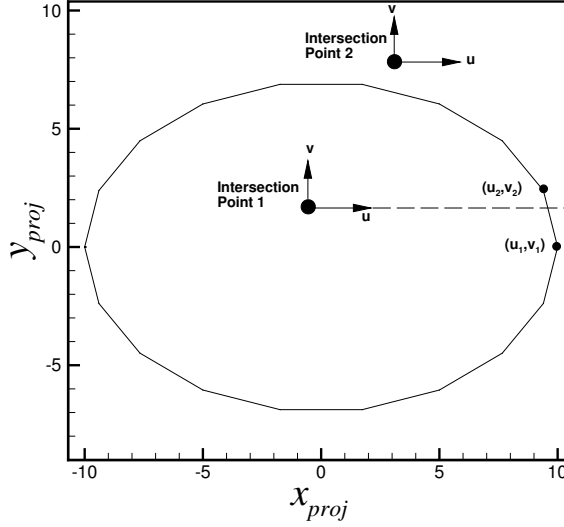
Figure 7. Example ray intersection in a two-dimensional projection.

observer location are used to calculate all angle parameters required for the diffraction coefficient of Eqn. 14. The complex value of the acoustic pressure field from the diffracted ray is then calculated using Eqn. 12. This process is repeated for each segment identified in the projected plane. A similar procedure is followed for the other types of diffracted rays.

For each source, observer, and airframe position the incident and diffracted rays are summed and their phase relationships are retained. For an observer location $\boldsymbol{O}$, the total complex amplitude of acoustic pressure from a monopole at source $\boldsymbol{S}$ is,

$$\hat{p}(\boldsymbol{O}) = \hat{p}_I(\boldsymbol{O}) + \sum \hat{p}_D(\boldsymbol{O}), \tag{28}$$

where $\hat{p}_I(\boldsymbol{O})$ is the complex pressure amplitude of the incident ray and $\hat{p}_D(\boldsymbol{O})$ are the complex pressure amplitudes of the diffracted rays (see Eqns. 12, 15, and 17). If the observer is in a shadow region, the incident ray is zero and the total diffracted field is the sum of all diffracted rays. Equation 28 is the tailored Green's function, g, with appropriate monopole source strength.

For particular source, observer, and airframe locations a discontinuity exists within the diffraction coefficient, D. The last terms of Eqn. 14 are,

$$\dots \frac{1}{\cos{(\nu\pi)} - \cos{(\nu\,(\phi_s - \phi_o))}} + \frac{1}{\cos{(\nu\pi)} - \cos{(\nu\,(\phi_s + \phi_o + \pi))}}. \tag{29}$$

Which are singular when $\phi_s - \phi_o = \pm\pi$ or $\phi_s + \phi_o + \pi = \pm\pi$, where ϕ_s and ϕ_o are the polar angles of the incident ray and the diffracted ray, as shown in Fig. 4, respectively. For example, $\phi_s = 3\pi/2$ results in a discontinuity. Here, the denominator of the first term in Eqn. 29, decreases as ϕ_o approaches $\pi/2$ which is directly below the diffraction point. In this case, values of ϕ_o less than $\pi/2$ are in the shadow region. To correct for the discontinuity, terms in Eqn. 29 are multiplied by a damping function to change the behavior from $\pm\infty$ to 0^+ and 0^- respectively as the denominator approaches zero. The damping function does not alter the terms far from the neighborhood of the singularity. The proposed functions for multiplication of the first and second term of Eqn. 29 are,

$$f_1 = 1 - \exp\left[-\delta\left\{\cos[\nu\pi] - \cos[\nu(\phi_o - \phi_s)]\right\}^2\right], \tag{30}$$

and,

$$f_2 = 1 - \exp\left[-\delta\left\{\cos[\nu\pi] - \cos[\nu(\phi_o + \phi_s + \pi)]\right\}^2\right], \tag{31}$$

where δ is a damping coefficient. Figure 8 shows the corrected term when multiplied by f_1 for the first term in Eqn. 29. This example corresponds to $\phi_s = 3\pi/2$, $\nu = 5/9$, and $0 \leq \phi_o \leq \pi$. The uncorrected function is discontinuous at $\phi_o = \pi/2$ and the corrected function is continuous and finite. Note, there is little deviation between the two functions far from $\phi_o = \pi/2$. The narrow region affected by the correction function is dependent on the damping coefficient. Decreasing the value of δ increases the range of values affected by the damping function. A value of $\delta = 30$ yields results that agree with measurement and are shown in the next section. The coefficient δ is held constant for all comparisons.
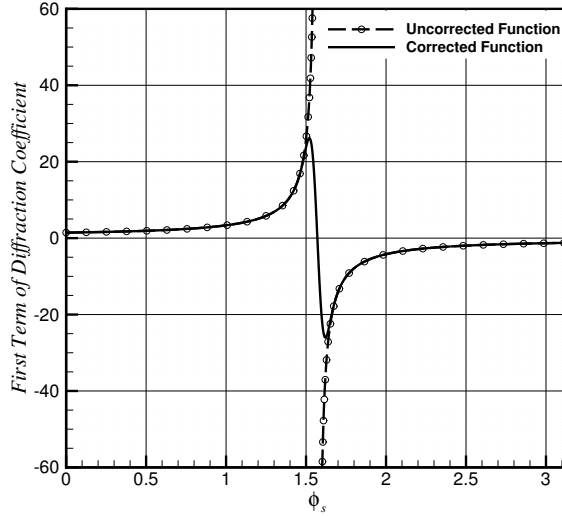
Figure 8. Example discontinuity correction.

4 Results

4.1 Steady RANS Solutions

Steady RANS solutions are examined to study the aerodynamics and turbulent statistics of free and installed jets. The solutions are compared with PIV of free and installed jets The steady RANS equations are solved with a computational fluid dynamics (CFD) approach using the NASA Fully Unstructured Navier-Stokes three-dimensional [79] (FUN3D) solver. The Menter [80] shear stress transport (SST) turbulence model is used to close the RANS equations. The model utilizes the strengths of the Jones and Launder k-ϵ model [81] and the Wilcox k-ω model [82,83]. In this work, the noise source is dependent upon quantities obtained from the steady RANS solution.

The coordinate system and geometry of the nozzle and plate are illustrated in Fig. 9. Coordinates x, y, and z are normalized by the nozzle exit diameter, D. The origin of the coordinate system is the center of the nozzle exit. The positive x-axis is the jet centerline, the y-axis is normal to the plate, and the z-axis is parallel to the plate. The plate is located multiple nozzle diameters from the jet centerline axis, y_p, and multiple nozzle diameters from the nozzle exit to the trailing edge, x_p.
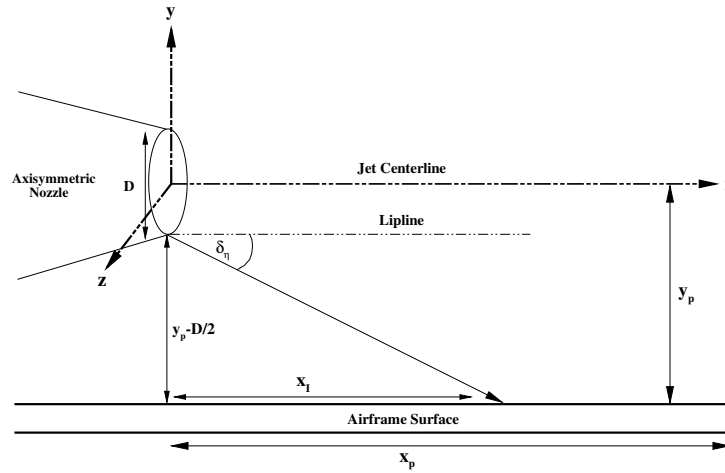
Figure 9. The coordinate system.

The plate positions examined relative to the nozzle exit are shown in Table 1. The first column contains normalized streamwise distances from the nozzle exit to the edge of the flat plate and the second column shows normalized radial distances to the flat plate. Table 2 shows the jet operating conditions examined for each plate position. For each operating condition, free and installed jet steady RANS solutions are obtained. The operating conditions include five subsonic jets, a transonic jet, and three supersonic jets. Four of the conditions are heated. The nozzle geometries, flow conditions, and plate positions coincide with the PIV measurements of Bridges and Wernet [52].

The computational domain consists of a mixed element (structured-unstructured) grid. An

19

Table 1. Plate Locations.

Axial Distance (x_p/D)	Radial Distance (y_p/D)
4	1, 2, 4, 6, 8, 10
10	1, 2, 4, 6, 8, 10
20	1, 2, 4, 6, 8, 10

Table 2. Jet Operating Conditions.

Nozzle	Setpoint	NPR	TTR	M_j
SMC000	3	1.197	1.000	0.513
SMC000	7	1.861	1.000	0.985
SMC000	23	1.102	1.814	0.376
SMC000	27	1.357	1.926	0.678
SMC000	29	1.888	2.118	1.000
SMC000	46	1.219	2.862	0.548
SMC016	11606	2.733	1.000	1.290
SMC016	11610	3.670	1.000	1.500
SMC016	11617	4.320	1.000	1.610

unstructured grid is used to resolve the flow around the airframe and a structured grid is used to resolve the jet plume. All the CFD calculations are three-dimensional. Symmetry of the steady RANS solution and computational domain allow for large computational savings. Figure 10 shows an outline of the three-dimensional computational domain with the plate located two nozzle diameters, D, off-set from the jet axis and parallel to the jet centerline ($y_p/D = -2$). p_o and T_o, calculated from the nozzle pressure ratio (NPR) and TTR, are specified at the nozzle inlet plane. The ambient static pressure is held constant at the far-field boundary. A symmetric boundary condition is enforced on the x-y plane at $z = 0$. All other boundaries are defined with a free-stream condition of $M_\infty = 0.01$ and ambient pressure. The SMC000 nozzle profile and a portion of the computational domain are shown in Fig. 11. This portion of the domain represents a slice in the x-y plane at $z = 0$ normalized by D. The full computational domain extends $75D$ downstream, $100D$ cross-stream along the y-axis, and $50D$ cross-stream along the z-axis. This forms a rectangular prism. Note that the far-field z plane boundary condition implies a symmetric flow solution. Typically, the number of grid points in the computational domain with the plate present is approximately 2.2 million and the number of elements is approximately 2.8 million. The number of grid points in the computational domain with only the nozzle present is approximately 1.2 million and the number of elements is approximately 1.5 million.

Validation of the free jet steady RANS solution is performed by comparing the streamwise velocity component, $\overline{u}$, and turbulent kinetic energy, k, with the PIV measurements of Bridges and Wernet [52]. Here, mean velocities, k, and Reynolds stresses are important statistics for noise prediction. We present the first two for validation of the steady RANS solutions and in subsequent analysis.

A comparison of the steady RANS solution of a subsonic cold jet operating at $M_j = 0.513$ from the convergent SMC000 nozzle is shown in Fig. 12. Here, contours show qualitative differences of $\overline{u}$ and k. $\overline{u}$ and k are normalized by the fully expanded velocity and its square, respectively. The
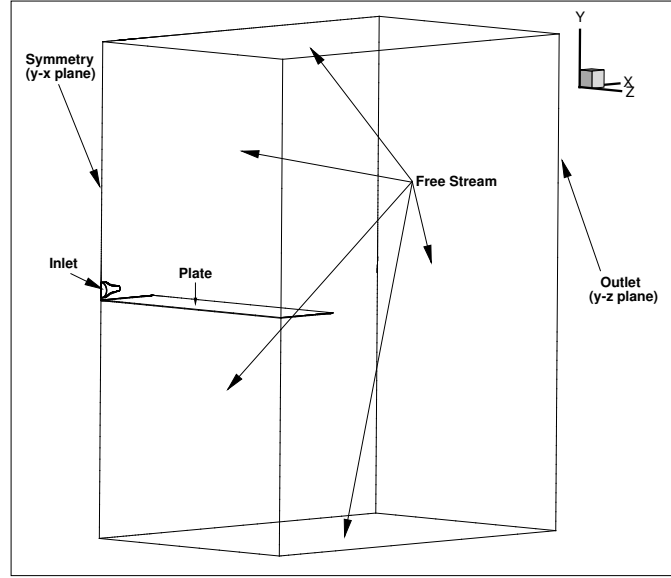
Figure 10. An outline of the computational domain used for the CFD calculations. The flow of the jet is in the positive x direction.
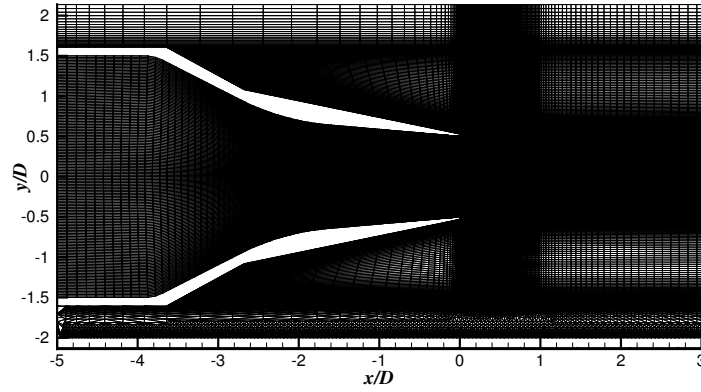

Figure 11. A portion of the computational domain on the x-y plane at $z = 0$ showing the structured/unstructured grid of the convergent nozzle and flat plate located $2D$ from the centerline.

steady RANS solutions are shown on the top half planes and the corresponding PIV data are shown on the bottom half planes. Note that the measured data near the nozzle exit is not available due to the placement of the PIV cameras and flow seeding. $\bar{u}$ as shown in Fig. 12(a) has noticeable variation from the PIV. The predicted thickness of the potential core past $6D$ is smaller than measurement and the fall-off past $8D$ is higher. The predicted peak k occurs near $5.5D$ and the PIV peak k occurs further downstream at $6.25D$. Furthermore, the predicted magnitude of peak k is smaller than measurement. However, the global qualitative agreement compares favorably with other solutions produced by similar CFD codes (for example see Georgiadis et al. [84]).
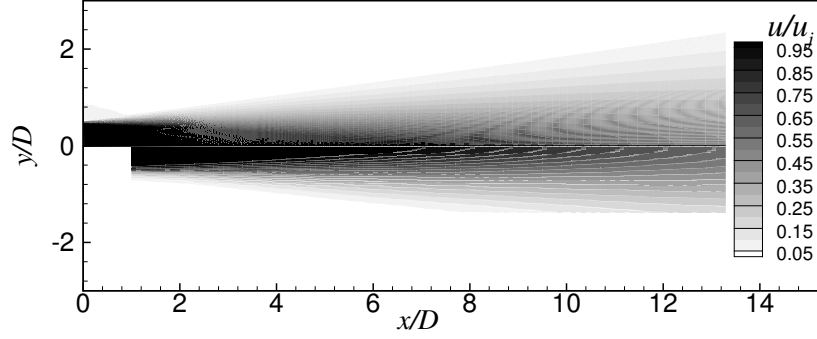
(a) Normalized streamwise component of velocity.
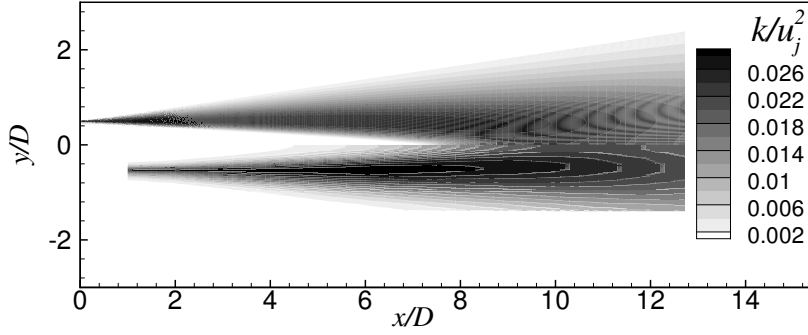
(b) Normalized turbulent kinetic energy.

Figure 12. Contours of the steady RANS solution and PIV data. The steady RANS solutions are shown on the top half planes and PIV data are shown on the bottom half planes. The jet operates at $M_j = 0.513$ and TTR $= 1.00$.

Comparisons are conducted for the free jet by examining aerodynamic data along the centerline and axial locations at $x/D = 1, 4$, and 16. Figure 13 shows the centerline variation of $\bar{u}/u_j$ and k/u_j^2 of both the steady RANS solution and PIV data. Figure 14 shows radial profile comparisons of the same quantities. In Fig. 13(a), the predicted jet potential core length is larger than measurement by $2D$. The predicted $\bar{u}$ follows the same approximate $1/x$ decay as the measured data along the centerline, shown in Fig. 13(a), and also matches the radial decay at $x/D = 1$ and 4, shown in Fig. 14(a). Predicted k along the centerline matches the measurement in terms of peak magnitude but the peak occurs one diameter further upstream than measurement. The peak magnitudes of

k at $x/D = 1$ and $x/D = 4$ are larger than measurement by 0.0015 and 0.001 k/u_j^2 respectively and are located $0.25D$ closer to the centerline than experiment. The solution under-predicts both $\overline{u}$ and k relative to measurement far downstream from the nozzle exit.

(a) Streamwise velocity component, $\overline{u}$.   (b) Turbulent kinetic energy, k.
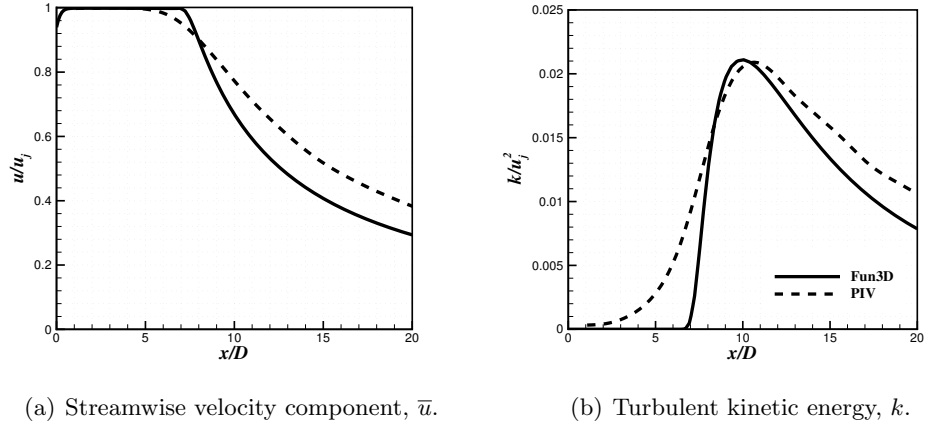
Figure 13.   The steady RANS a) $\overline{u}$ and b) k along the jet centerline compared with the measurement of Bridges and Wernet [52]. The jet operates at $M_j = 0.513$ and TTR $= 1.00$ from the convergent SMC000 nozzle.

Comparisons are presented for the supersonic over-expanded jet operating at $M_j = 1.29$ from the $M_d = 1.5$ convergent-divergent SMC016 nozzle. Again, the aerodynamic data is shown along the centerline and radial locations at $x/D = 1, 4$, and 16. Figure 15 shows the centerline variation of normalized $\overline{u}$ and k of both the steady RANS solution and PIV. Figure 16 shows radial profile comparisons of the same quantities. As observed in Fig. 15, the predicted potential core length is approximately $2D$ larger relative to measurement. Within the potential core, the predicted shock-cell structure location compares favorably with measurement. The steady RANS solution over-predicts the rate of decay along the centerline as shown in Fig. 15(a) and matches the radial decay in the potential core region at $x/D = 1$ and 4 as shown in Fig. 16(a). The steady RANS solution under-predicts the radial decay through the shear layer greater than $0.5D$ from the centerline. In the fully developed region of the flow at $x/D = 16$, the steady RANS solution only slightly over-predicts the radial velocity profile. This is a favorable prediction relative to the k profile at $x/D = 16$ shown in Fig. 16(b) and the subsonic jet predictions shown at $x/D = 16$ in Fig. 14. On the centerline, peak k/u_j^2 is approximately 0.003 below measurement and occurs $2D$ further downstream than measurement as shown in Fig. 15(b). The k prediction agrees with experiment in peak magnitude at $x/D = 4$ but over-predicts $k/u_j{}^2$ at $x/D = 1$ and $x/D = 16$ by 0.015 and 0.005, respectively. Like the subsonic cold jet radial comparisons of k, radial comparisons at far downstream locations over-predict measurement. These trends are representative of all jet conditions shown in Table 2. The predictions are favorable relative to measurement based upon this author's experiences with steady RANS solutions for the jet conditions examined, especially so in the potential core region of the flow-field where inviscid terms dominate the equations of motion.

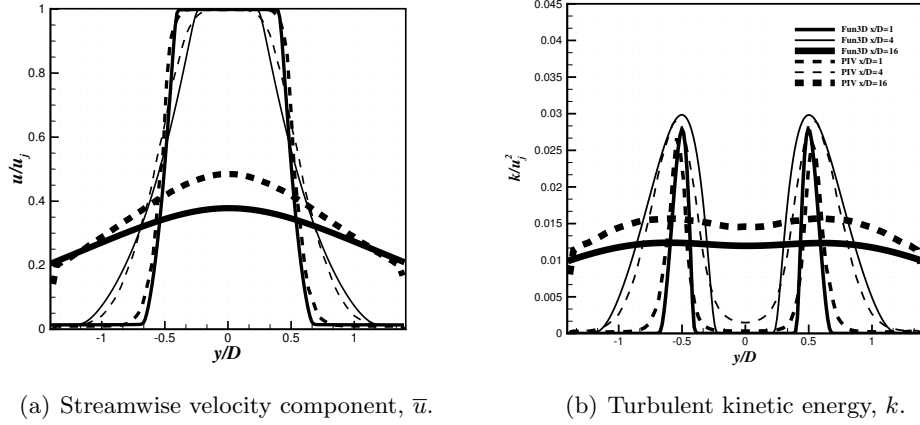The steady RANS solutions of a $M_j = 0.513$ and TTR $= 1.00$ jet from the convergent SMC000

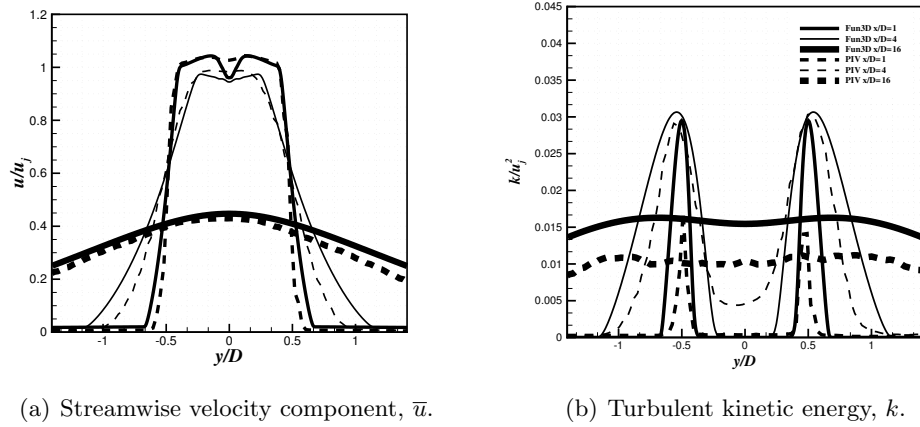(a) Streamwise velocity component, $\overline{u}$. (b) Turbulent kinetic energy, k.

Figure 14. Radial profiles of steady RANS a) $\overline{u}$ and b) k compared with the measurement of Bridges and Wernet [52]. The jet operates at $M_j = 0.513$ and TTR $= 1.00$ from the convergent SMC000 nozzle.

nozzle in the presence of a flat plate are now compared with the free jet operating at the same condition. Figure 17 shows radial profiles of k at $x/D = 10$ for multiple plate positions. The plate is located at $y_p/D = -1, -2, -4, -6, -8$, and -10 perpendicular to the jet centerline and extends to $x_p/D = 10$ and 20 downstream from the nozzle exit. Figure 17 shows that as the plate is moved closer to the jet the k distribution is increasingly deformed. The peak magnitude closest to the plate decreases and the peak magnitude furthest from the plate increases. This trend is amplified when increasing the x_p/D location from 10 to 20 for most of the cases examined. Furthermore, the jet plume is being deformed and is drawn toward the plate due to a coanda like effect. For example, in Fig. 17(a) the $x_p/D = 10$ and free jet case both have a k local minimum at $y/D = 0$. However, as the plate is moved closer as in Fig. 17(f) the local minimum of k for $x_p/D = 10$ is now located at $y/D = -0.16$. The effect of extending the plate from $x_p/D = 10$ to $x_p/D = 20$ amplifies the effect of the deformation of the jet plume as shown in Fig. 17(a). The peak k close to the plate is lower by 0.0005 $k/u_j{}^2$ and the peak k furthest from the plate is higher by 0.001 $k/u_j{}^2$. Similar changes of the k distribution are observed for all jet conditions examined. These numerical results show the changes in the aerodynamic characteristics of the jet plume induced by nearby surfaces. These changes affect the noise source intensity and position as the plate location is altered.

(a) Streamwise velocity component, $\overline{u}$. (b) Turbulent kinetic energy, k.
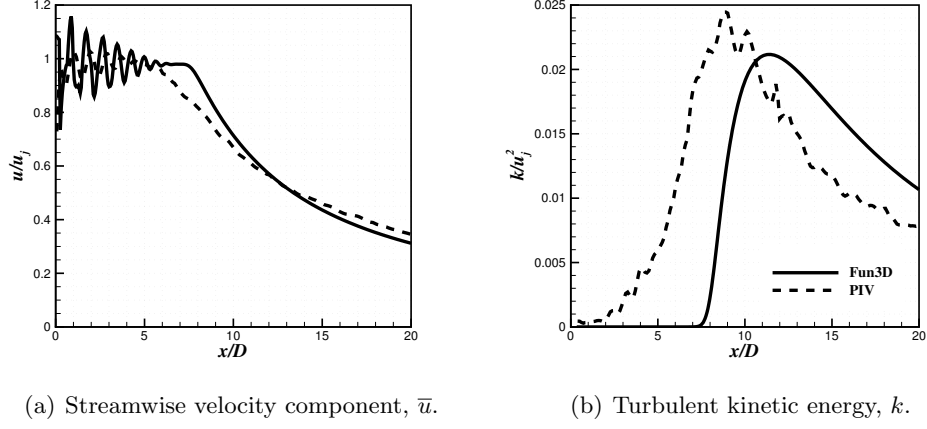
Figure 15.   The steady RANS a) $\overline{u}$ and b) k along the jet centerline compared with the measurement of Bridges and Wernet [52]. The jet operates at $M_j = 1.29$ and TTR = 1.00 from the SMC016 nozzle.

(a) Streamwise velocity component, $\overline{u}$. (b) Turbulent kinetic energy, k.

Figure 16.   Radial profiles of steady RANS a) $\overline{u}$ and b) k compared with the measurement of Bridges and Wernet [52]. The jet operates at $M_j = 1.29$ and TTR = 1.00 from the SMC016 nozzle.
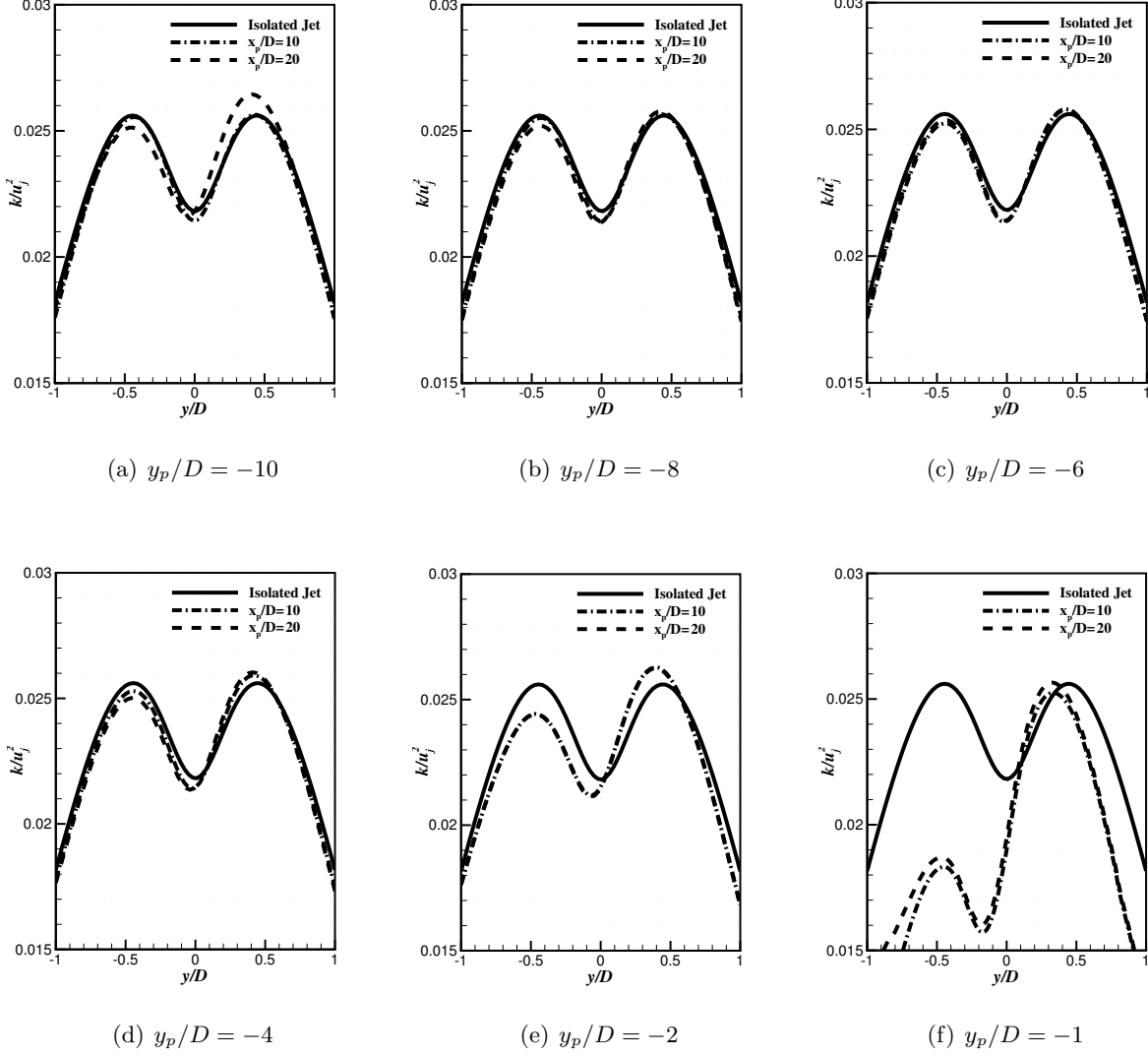
Figure 17.   Radial variation of k at $x/D = 10$ due to a jet operating at $M_j = 0.513$ and TTR = 1.00. Parts a) through f) show solutions at $y_p/D = -10$, -8, -6, -4, -2, and -1 and $x_p/D = 10$ and 20 ($D = 0.0508$ m).

4.2 The Variation of Γ with Jet Operating Condition and Airframe Position

The results of the aerodynamic assessment show that nearby solid surfaces change the aerodynamic characteristics of the jet flow-field, even if the jet centerline is many diameters from a surface. Thus, the method by which a jet engine is integrated with the airframe of a flight vehicle can have significant effect on the aerodynamic source of sound. This is a highly complicated problem that has received significant attention (see Czech [4] and Thomas [3,85] for example). It is characterized by a large number of parameters that are highly interdependent. In this section, the model of Tam and Auriault [19] is used to quantify the relative effect of propulsion airframe aeroacoustics installation effects on the aerodynamic source. Γ is used as a basic guide to ascertain whether the aerodynamic source is affected by the airframe relative to the equivalent free jet aerodynamic source.

The model for spectral density, S, of Tam and Auriault [19] is,

$$S(\boldsymbol{x},\omega) = 4\pi \left(\frac{\pi}{\ln 2}\right)^{3/2} \int_{-\infty}^{\infty} \int_{-\infty}^{\infty} \int_{-\infty}^{\infty} \frac{\hat{q}_s^2 l_s^3}{\overline{c}^2 \tau_s} \frac{|p_a(\boldsymbol{x};\boldsymbol{y},\omega)|^2 \exp\left[-\frac{\omega^2 l_s^2}{\overline{u}^2 4 \ln 2}\right]}{1 + \omega^2 \tau_s^2 \left(1 - \frac{\overline{u}}{c_\infty}\cos\theta\right)^2} d\boldsymbol{y}, \tag{32}$$

where $\hat{q}_s = (4/9)A^2\overline{c}^2\overline{\rho}^2 k_s^2$ is a statistical source term and k_s is associated with turbulence that produces fine-scale mixing noise. A is a constant coefficient, c is the speed of sound, $\overline{u}$ is the mean streamwise velocity component, $\boldsymbol{x}$ is the observer position, $\boldsymbol{y}$ is the source position, and ω is the radial frequency. k_s is set equal to k computed from the steady RANS solution.

If predictions are restricted to the sideline direction and it is assumed that sound refraction by the jet shear layer has negligible effect on S, then a simplified form of $p_a(\boldsymbol{x};\boldsymbol{y},\omega)$ can be constructed. As shown by Morris and Farassat [20], the adjoint acoustic pressure at $\Psi = 90$ deg. (the jet sideline at $\Phi = 90$ deg.) is, $|p_a(x_2;\boldsymbol{y},\omega)|^2 = \omega^2/(64\pi^4 c_\infty^4 x^2)$. The scales of turbulence in Eqn. 32 are related to the steady RANS solution of the jet by simple dimensional models. The coefficients are calibrated with the SMC000 nozzle operating at $M_j = 1.00$ and TTR = 1.00. The values are $A = 3548$, $c_l = 0.018$, and $c_\tau = 0.015$, and vary from those calculated by Tam and Auriault [19] because the steady RANS solver and turbulence model differ.

The effects that the flat plate has on acoustic intensity originating from the jet aerodynamic source are investigated by using the steady RANS solutions and Tam and Auriault's model. The free jet predictions are subtracted from the installed jet predictions on a power spectral density (PSD) basis for comparison. The first comparison consists of the cold subsonic jet at $M_j = 0.513$ and is presented in Fig. 18. In Fig. 18(a), the plate is located at $y_p/D = -1, -2, -4, -6, -8$, and -10 from the jet centerline and extends $x_p/D = 10$ downstream of the nozzle exit. In Fig. 18(b), the plate is located at $y_p/D = -1$ from the jet centerline and extends $x_p/D = 4, 10$, and 20 downstream of the nozzle exit. When the plate is $x_p/D = 10$ downstream of the nozzle exit, the trends in Fig. 18(a) show only a small effect on the noise spectrum as the plate approaches the centerline until the plate is at $y_p/D = -2$. The noise deviation from the free jet reaches a maximum of -1.2 dB at the lowest frequency and 0.75 dB at the highest frequency when the plate is located at $y_p/D = -2$. For all plate locations further than $2D$ from the centerline, the noise deviations are within ± 0.75 dB relative to the free jet case. When the plate is located at $y_p/D = -1$, the noise intensity is -6.9 dB relative to the free jet case at the lowest frequency. The effect of varying the plate length relative to the nozzle exit is displayed in Fig. 18(b). At the lowest frequency, the noise intensity deviation from the free jet reaches a maximum of -6.5 dB, -6.9 dB, and -7.9 dB as the plate is extended to $x_p/D = 4, 10$, and 20 downstream from the nozzle exit, respectively. At the highest frequency, the maximum deviation for each plate extension does not exceed 0.75 dB.
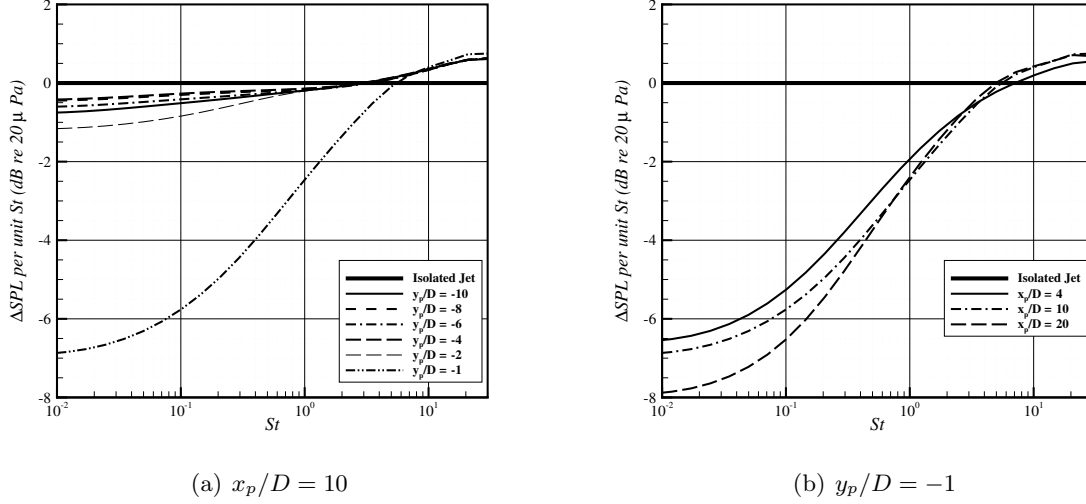
(a) $x_p/D = 10$ (b) $y_p/D = -1$

Figure 18. Predicted attenuation using the model of Tam and Auriault [19] for the free and installed jet at $R/D = 100$ and $\Psi = 90$ deg. The jet operates at $M_j = 0.513$ and TTR $= 1.00$ from the convergent SMC000 nozzle with exit diameter $D = 0.0508$ m. Part a) shows plate locations at $y_p/D = $ -1, -2, -4, -6, -8, and -10 laterally from the jet centerline and $x_p/D = 10$. Part b) shows the plate located at $y_p/D = $ -1 and $x_p/D = $ 4, 10, and 20.

An over-expanded supersonic $M_j = 1.29$ jet from the convergent-divergent SMC016 nozzle at various plate positions is now examined. A comparison is shown in Fig. 19(a) for the variation of ΔSPL as the surface approaches the jet centerline. Figure 19(b) shows the effect that the surface has on ΔSPL as the plate length is extended relative to the nozzle exit. In Fig. 19(a), the noise intensity deviation from the free jet reaches a maximum of -1 dB at the lowest frequency and 0.1 dB at the highest frequency when the plate is located at $y_p/D = -2$. For all plate locations further than $2D$ from the centerline, the noise deviations are within -0.6 dB relative to the free jet case at the lowest frequency and -0.02 dB at the highest frequency. When the plate is located at $y_p/D = -1$, the noise reaches a maximum -6.4 dB difference relative to the free jet case. In Fig. 19(b), the noise deviation relative to the free jet reaches a maximum of -5.7 dB, -6.4 dB, and -7.7 dB at the lowest frequency as the plate extends $x_p/D = 4, 10,$ and 20 downstream from the nozzle exit, respectively. The maximum dB difference relative to the free jet for each plate position is slightly smaller in magnitude at lower frequencies relative to the subsonic jet. There is no increase in noise intensity at high frequencies in contrast to the subsonic case.

The comparisons described are representative of the other jet conditions analyzed in this study. As the jet approaches the plate there is a consistently larger difference in the noise spectrum relative to the free jet at lower frequencies. This is due to the surface having a larger effect on the flow further downstream from the nozzle exit. It has been shown by Brooks et al. [86] and Podboy [87], for example, that peak noise sources are located near the nozzle exit at higher frequencies and lower frequency peak noise sources are located multiple nozzle diameters downstream. The presence of the plate has a larger effect on the jet flow multiple diameters from the nozzle exit and therefore has a larger effect on the aerodynamic source at lower frequencies.
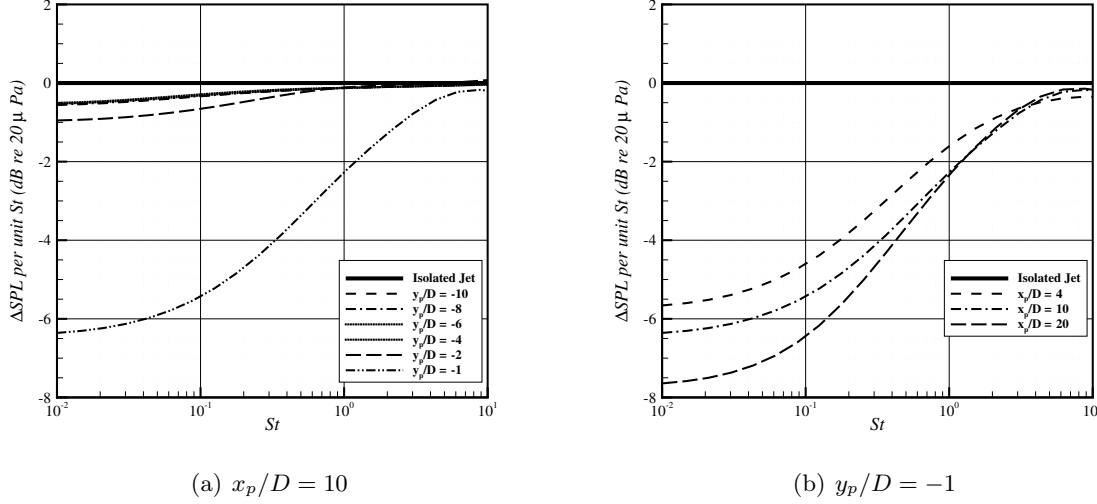
(a) $x_p/D = 10$

(b) $y_p/D = -1$

Figure 19.   Predicted attenuation using the model of Tam and Auriault [19] for the free and installed jet at $R/D = 100$ and $\Psi = 90$ deg. The jet operates at $M_j = 1.29$ and TTR $= 1.00$ from the convergent SMC016 nozzle with $D = 0.0508$ m. Part a) shows plate locations at $y_p/D = $ -1, -2, -4, -6, -8, and -10 laterally from the jet centerline and $x_p/D = 10$. Part b) shows the plate located at $y_p/D = $ -1 and $x_p/D = $ 4, 10, and 20.

Next, the effect of the plate on the spatial location of the acoustic source is examined by comparing contours of source intensity with varying plate position. This is accomplished by evaluating the integrand of Eqn. 32. Contours of SPL per unit St for the cold subsonic $M_j = 0.513$ jet at a frequency of 1 kHz ($St \approx 0.3$) are shown in Fig. 20. In this comparison the plate length extends to $x_p/D = 10$ and the plate is located at $y_p/D = -10, -6, -4, -2$, and -1 from the jet centerline. When the plate is located at $y_p/D = -10$ in Fig. 20(a), the noise source distribution is unaffected by the presence of the plate. The two peak noise sources are located $9.5D$ downstream from the nozzle exit and are symmetric in magnitude about the jet centerline. There is no significant deformation of the source distribution due to the presence of the plate further than $2D$ from the jet centerline. As the plate approaches the jet at $y_p/D = -2$, as shown in Fig. 20(d), the peak magnitude of the source closest to the plate is decreased by approximately 1 dB and the location is unchanged. When the plate is located at $y_p/D = -1$, as shown in Fig. 20(e), the peak noise source furthest from the plate is decreased in magnitude by approximately 1 dB and is shifted $0.5D$ upstream relative to the $y_p/D = -10$ case shown in Fig. 20(a). The peak noise source distribution closest to the plate is significantly deformed. The peak magnitude is decreased by approximately 6 dB and is shifted $1D$ upstream relative to the $y_p/D = -10$ case. An additional strong noise source is formed close to the plate further downstream at $x/D = 14$. This is a distinguishable difference from the other comparisons and is due to an increase in k past the trailing edge of the plate. Figure 20 shows that the magnitude of the peak acoustic source closest to the plate decreases as the plate surface approaches the jet centerline, and the magnitude of the peak acoustic source furthest from the plate is not significantly altered until the plate is located at $y_p/D = -1$. The location of the peak noise sources is unaltered until the plate is located at $y_p/D = -1$. Varying the azimuthal angle, Φ, will have little effect on the results using this analysis. These comparisons

29

represent trends that are consistent for the other jet conditions analyzed.

Overall, the results show that the plate has a larger effect on the acoustic source as it approaches the jet centerline and as the plate length extends further downstream. As the effective jet impingement area of the plate is increased, the acoustic intensity radiating from the jet mixing noise decreases. Note, this does not account for additional sources produced by the jet interacting with the surface.
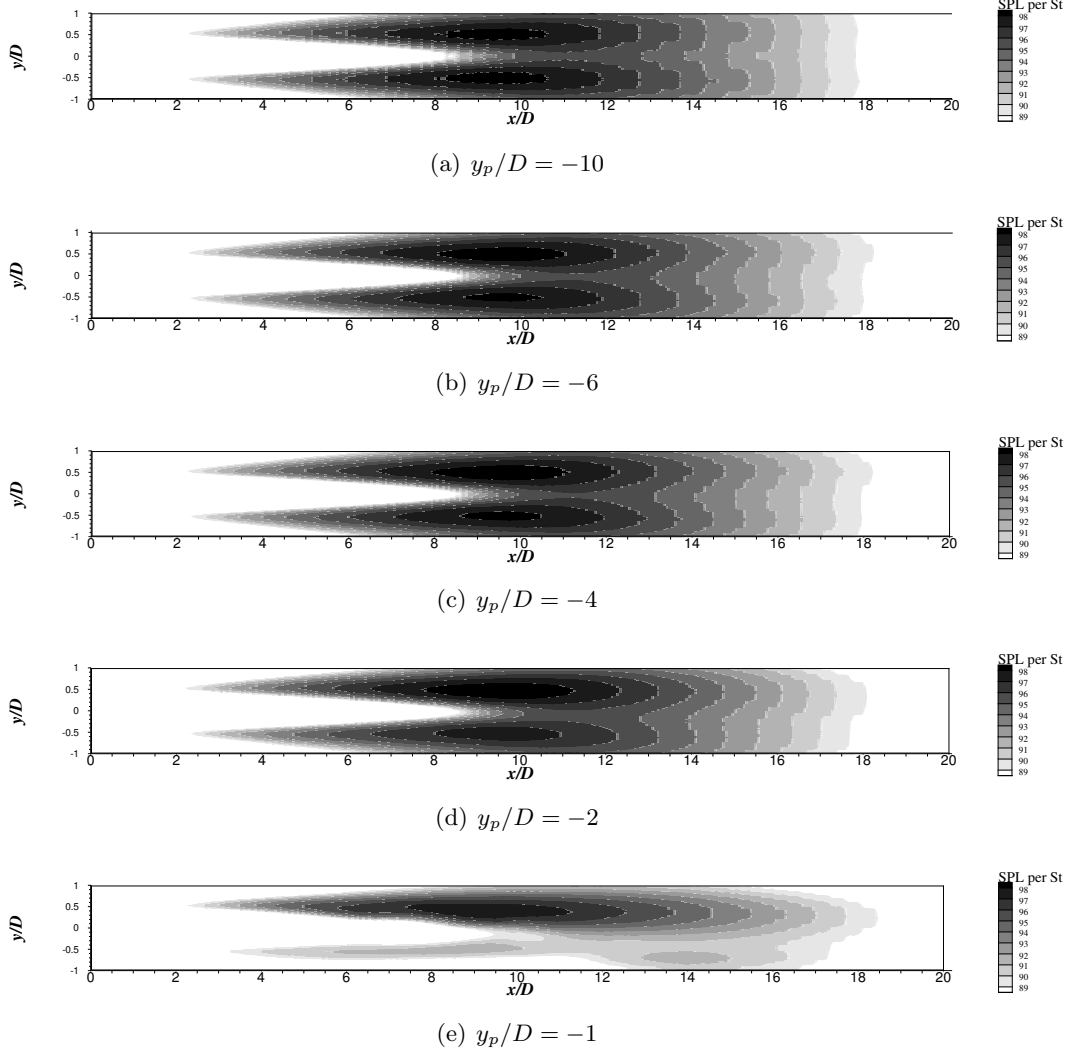

(a) $y_p/D = -10$

(b) $y_p/D = -6$

(c) $y_p/D = -4$

(d) $y_p/D = -2$

(e) $y_p/D = -1$

Figure 20. Contours of acoustic source strength at $f = 1000$ Hz ($St \approx 0.3$). The jet operates at $M_j = 0.513$ and TTR $= 1.00$. Parts a) through e) show the acoustic source with the plate located at $y_p/D = -10$, -6, -4, -2, and -1 respectively and $x_p/D = 10$.

The non-dimensional number Γ is used to quantify the effect of a nearby surface on the jet noise source. The overall sound pressure level (OASPL) is predicted over a frequency range of 20 Hz to 100 kHz using the steady RANS solutions and Eqn. 32 at $\Psi = 90$ deg. The installed jet predictions of OASPL are subtracted from the free jet predictions on a PSD basis. Figure 21 shows the absolute value of ΔOASPL as a function of Γ. The data collapse shows a critical value of Γ

of approximately unity. As the cross-stream length scales $y_p(y_p - D/2)$ decrease to the equivalent of the product of the jet and airframe length scales $(D_j x_p \tan[\delta_\eta])$, Γ increases from 0 to 1. In Fig. 21, small values of Γ approaching approximately 1 have ΔOASPL less than 0.5 dB and are considered negligible. As the jet spreading angle, fully expanded jet diameter, or surface length increase, the product of the jet and airframe length scales surpasses the cross-stream length scales and Γ increases beyond unity. As a result of the dominance of the jet and airframe length scales in this region, $1 < \Gamma < \infty$, the physical quantities of the aerodynamic flow are sufficiently altered and have a large effect on the jet noise source. As shown in Fig. 21, values of $\Gamma > 1$ result in a range of ΔOASPL from 2 dB to 2.75 dB. It is observed that ΔOASPL increases as Γ increases.
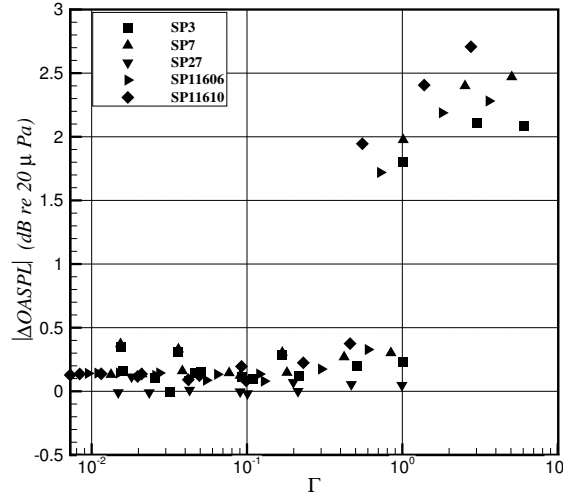
Figure 21. ΔOASPL, relative to the free jet, for each condition shown in Tables 1 and 2.

When $\Gamma << 1$, the airframe is expected to have a negligible effect on the jet noise source. For instance, a supersonic on-design $M_j = 1.5$ cold jet with an airframe surface located at $x_p/D = 20$ and $y_p/D = 4$ corresponds to $\Gamma \approx 0.099$ and ΔOASPL $= 0.083$ dB in Fig. 21. Since $\Gamma << 1$ and there is a negligible difference relative to the free jet noise source, the free jet aerodynamic source model along with a tailored Green's function can be used for a prediction that includes propagation about the airframe. For example, a $M_j = 0.985$ jet with an airframe surface located at $x_p/D = 4$ and $y_p/D = -1$ corresponds to $\Gamma = 5.063$ and ΔOASPL $= 2.47$ dB in Fig. 21. For large values of Γ, some noise reduction is attributed to the change in the jet noise source and not to shielding effects.

The parameter Γ can include additional terms involving multiple jet streams or account for the boundary layer thickness on the airframe. An equivalent parameter for the fully expanded jet diameter and jet spreading angle can be developed for a dual-stream jet. However, a new model will be required for the estimation of the jet spreading angle. Inclusion of boundary layer effects will increase the effect of the cross-stream length scales. The airframe boundary layer thickness can be subtracted from the cross-stream length scales. A model to estimate the boundary layer thickness would be required. The general effect of the airframe on the jet noise source as a function of Γ is expected to be consistent for these cases but would likely have a different critical value.

4.3 Acoustic Validation

4.3.1 Ray Tracing Validation

This section describes comparisons of predicted and measured shielding of a point source by rectangular plates. Measurements of Ahtye and McCulley [53] are used to validate the ray tracing method and its implementation. Unfortunately, the measured data is not available in a digital form and is digitized electronically from technical reports. There is some error due to the digitization process. The predictions are also compared with NASA's Fast Scattering Code (FSC) developed by Tinetti and Dunn [49].

4.3.2 Measurement Overview

Rectangular plates and cylinders are used to validate the ray tracing method. Here, we focus on rectangular plates because of their sharp edges that are similar to airfoil trailing edges. The rectangular plates have square and sharp tapered edges. The angles of the square and sharp edge are $\beta = 270$ and 340 degs. The dimensions of the square and sharp edge are shown in Fig. 22. The length and width of the plates is $L = 2.0$ m and $W = 0.5$ m.

Figure 23 shows the coordinate system used for the point source validation. The point source is placed above the plate and is simulated with an inverse tapered horn connected to a loudspeaker. A microphone is used to conduct measurements at various locations along the x-axis below the plate. The microphone location on the traverse axis is designated by the angle θ relative to the source. $\theta = 0$ deg. is directly below the source and positive θ signifies a microphone position in the positive x direction. See Ahtye and McCulley [53] for a full description of the measurements, sound source, microphone, directivity, amplitudes, and calibration details. Ahtye and McCulley encountered a number of difficulties during their experiment. Notable difficulties include: simulating a pure omni-directional sound source, reflections from acoustic wedges lining the anechoic chamber walls, possible error in the simulated point source location, and impedance loading of the source by reflection from the plate. The sensitivity of the point source location relative to prediction will be discussed.

(a) Square Edge   (b) Sharp Edge
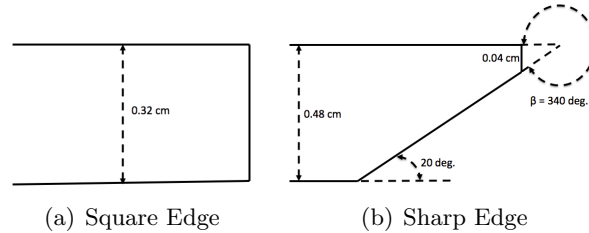
Figure 22. Rectangular plate edge dimensions.

Surface grids are created that correspond to the rectangular plates used in the measurement. The number of elements in the domain is 54 and the number of nodes is 80. Note, ray tracing solutions of rectangular geometry are independent of the number of nodes used. Figure 24 shows the surface grid, the calculated extracted edge, and the source location. The acoustic source used in the simulation consists of a stationary monopole of unit strength located at $x = 0$, $y = 0$, and $z = W/2$. After identifying the edge of the geometry, the incident and diffracted rays are determined for each microphone location, as shown in Fig. 25. The diffracted rays are summed for
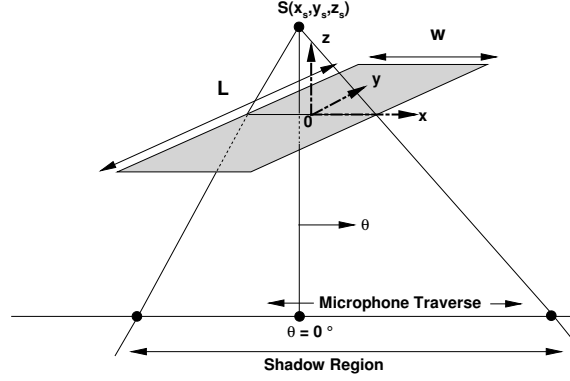
Figure 23. Coordinate system of the point source validation experiment.

the total complex acoustic pressure and converted to sound pressure level (SPL). The corresponding incident free-field is subtracted from the diffracted field to determine the shielding in ΔSPL.

The predicted and measured ΔSPL is shown as a function of the traverse angle, θ, at various frequencies. The traverse is located at $z = -10W$, $y = 0$, and ranges from $-4W \leq x \leq 4.5W$. The range of available measured data varies by case. Angles, $\theta = \pm 45$ deg., correspond to the edge of the geometric shadow region. The Helmholtz number, kW, is shown for each comparison, where k is the wave number and W is the width of the plate.
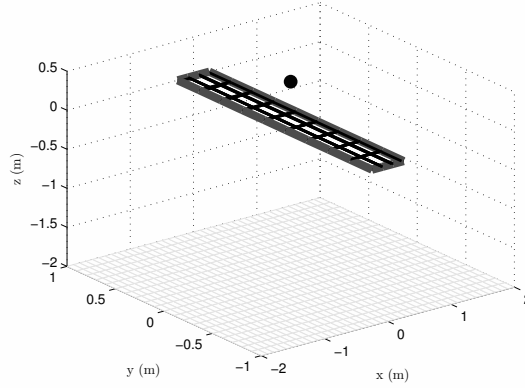
Figure 24. The diffraction edge is identified based on the source and observer location.

Comparisons of the square edge case, $\beta = 270$ deg., are shown in Fig. 26. The source excitation frequencies are 1, 2, 4, and 12 kHz. The predictions illustrate that the overall trends of diffraction are captured by ray tracing but with some noticeable error. The maxima and minima are generally coincident for all frequency ranges presented with exception of the highest frequency. The captured pattern of the diffracted field resembles the constructive and destructive interference between the multiple diffracted waves produced by the edges. Also, the predicted diffraction pattern is sym-

33
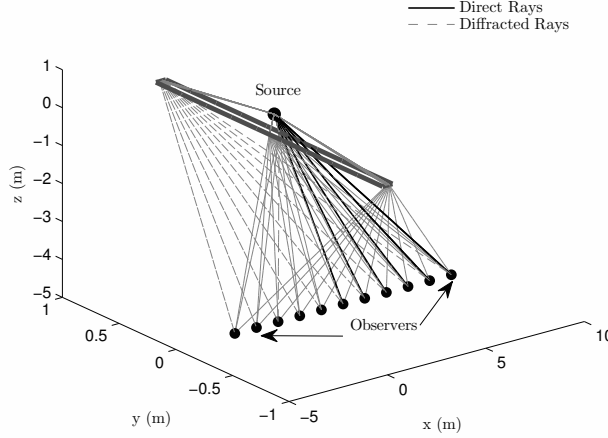
Figure 25. Incident and edge diffracted acoustic rays radiating from a monopole source above a flat plate.

metric, that is due to the geometry and source directivity symmetry. The slight asymmetry of the measured data is likely due to the difficulty of placing the source and its inherent directivity. The ray tracing method consistently under-predicts the measured shielding for all frequencies, where FSC over-predicts the shielding for 1, 2, and 4 kHz. The largest deviation from the ray traced and measured peaks ranges from 4-7 dB, except near $\theta = 45$ deg., while FSC over-predicts the measurements by 4-5 dB and is within ± 8 dB at 4 kHz. The discontinuous jump present in the ray tracing prediction at $\theta = 45$ deg. is due to the addition of direct rays to the diffracted field outside of the shadow region. These discontinuities in the diffracted field were also observed by Agarwal et al. [72].

Comparisons for a sharp edge case are shown in Fig. 27 where $\beta = 340$ deg. Measured data for this case are available at frequencies of 4 and 12 kHz. The discontinuity in the prediction is again apparent at $\theta = 45$ deg., where the shadow region ends. In contrast to the square edge case, the ray tracing predictions show improved agreement in terms of the shielding magnitude, especially at small angles. Within the range $|\theta| < 10$ deg., the ray tracing predictions are within $\approx \pm 3$ dB of the measurement at the intensity peaks and $\approx \pm 4$ dB at the minima. Ray traced predictions also agree well with the FSC prediction in this range. The larger deviation of the maxima and minima (> 5 dB) occur closer to the edge of the shadow region. Some of the deviation in this region is attributed to the discontinuity correction. Ray traced predictions are compared to FSC at $f = 1$ kHz and 2 kHz. At 1 kHz, the ray tracing prediction does not capture the same diffraction pattern as the FSC prediction but is in close agreement of the peak magnitude at $\theta = 0$ deg. This illustrates the low frequency limit of ray tracing. At 2 kHz, the prediction of the diffraction pattern generally agrees with the FSC prediction, except near the edge of the shadow zone. There is a 4 dB difference at the maxima and a much larger difference (> 10 dB) at the minima. The larger difference at the minima is due to a larger phase sensitivity for destructive wave interference.
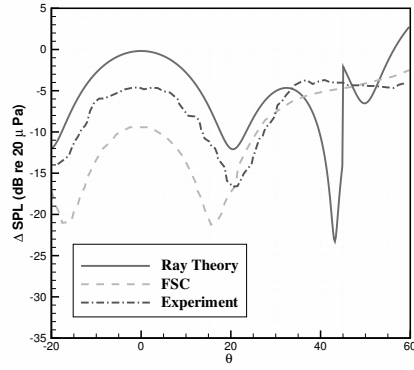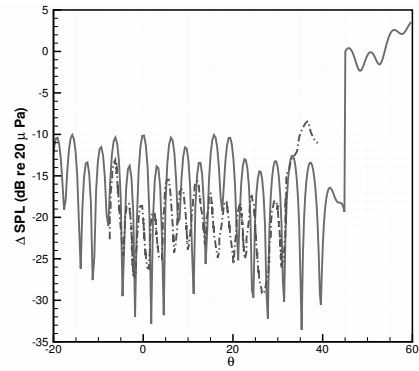
(a) $f = 1000$ Hz and $kW = 9$
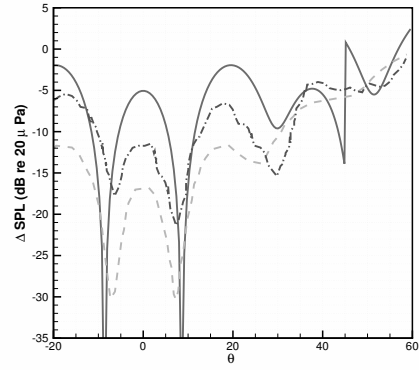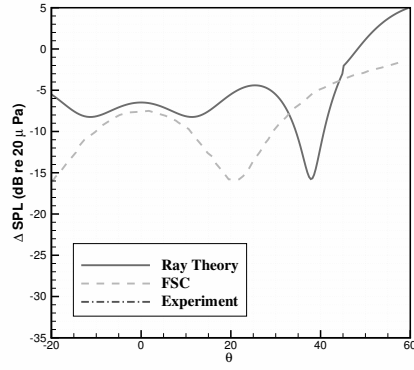
(b) $f = 2000$ Hz and $kW = 18$
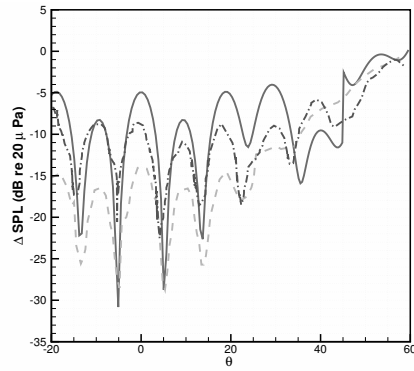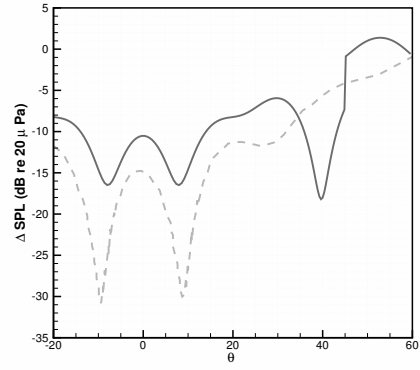
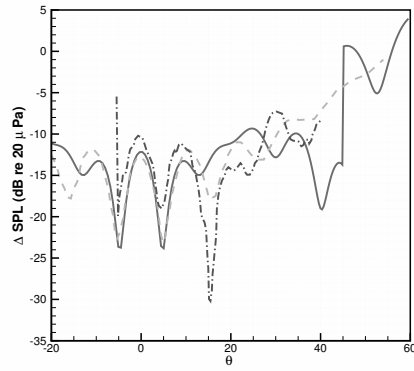(c) $f = 4000$ Hz and $kW = 37$

(d) $f = 12000$ Hz and $kW = 110$

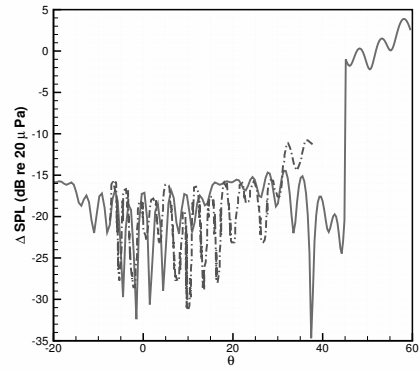Figure 26. Square edge shielding predictions compared to measurement with source at $x = 0$, $y = 0$, and $z = W/2$.

(a) $f = 1000$ Hz and $kW = 9$

(b) $f = 2000$ Hz and $kW = 18$

(c) $f = 4000$ Hz and $kW = 37$

(d) $f = 12000$ Hz and $kW = 110$

Figure 27. Sharp edge shielding predictions compared to measurement with source at $x = 0$, $y = 0$, and $z = W/2$.

4.3.3 Effect of Edge Angle

To quantify the effect of edge angle variation on the diffracted field, ray tracing predictions in the shadow region are examined while varying β. FSC and measurements are also shown at angles $\beta = 270$ and 340 degs. Figure 28 shows these comparisons at $f = 4$ kHz. Predictions demonstrate an increased shielding effect as edge angle increases. The magnitude of the constructive interference pattern decreases. The relative decrease and increase of the maxima and minima illustrate a flattening effect as the edge angle increases. There is a maximum 7 dB decrease in magnitude as the edge angle increases from $\beta = 270$ deg. to $\beta = 340$ deg. at $\theta = 0$ deg., resulting in an average 0.1 dB per deg. decrease. The relative magnitude difference from crest to trough decreases as $|\theta|$ increases. Measurement shows only a small difference in attenuation between the two angles. Interestingly, the FSC predictions do not follow the same trend as the ray tracing method. FSC predictions show an overall decrease in shielding for the sharp edge ($\beta = 340$ deg.) case. The relative difference in magnitude from peak to trough does decrease, which slightly mimics the flattening trend of the diffraction pattern demonstrated by the ray tracing method. Ray traced predictions show a stronger sensitivity to the sharp edge angle relative to FSC and measurement.
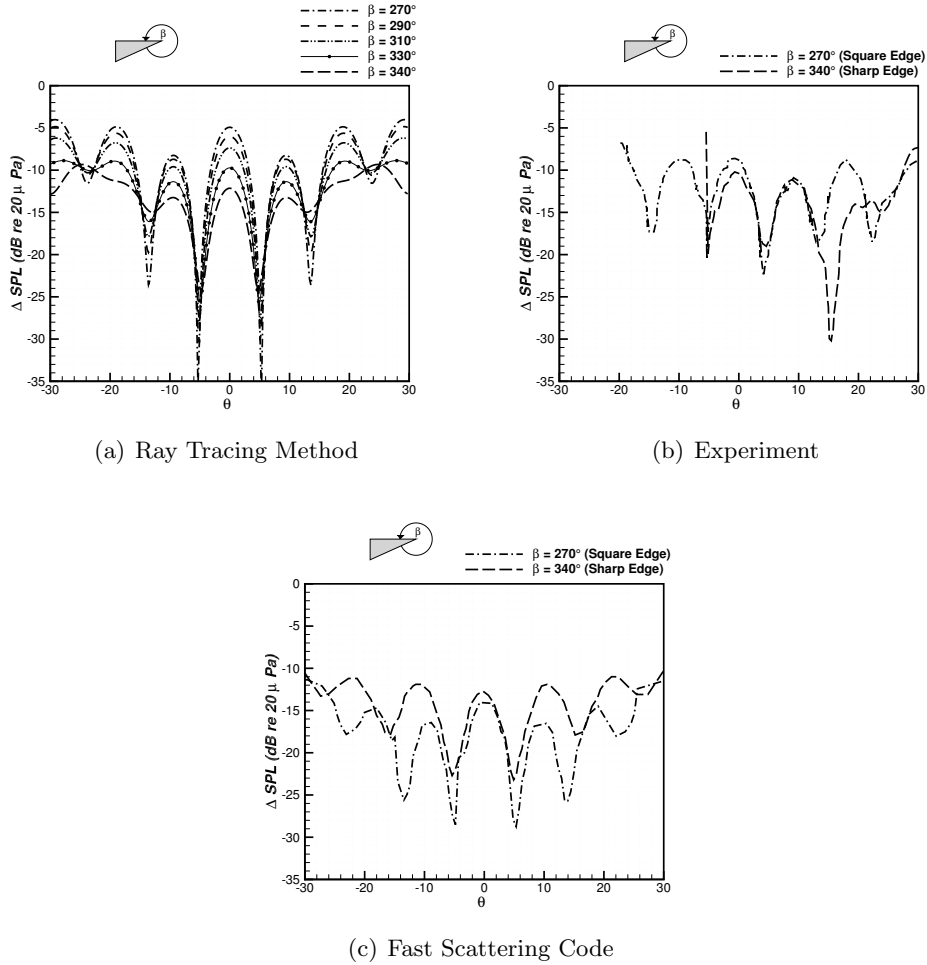

(a) Ray Tracing Method   (b) Experiment

(c) Fast Scattering Code

Figure 28.   Noise attenuation dependence on edge angle at $f = 4000$ Hz.

4.3.4 Point Source Sensitivity

In the experiment of Ahtye and McCulley [53], the opening at the small end of the inverse tapered horn has a diameter of $D_T = 6.3$ mm. This finite distance causes additional uncertainty when a point source is used with ray tracing predictions. At high frequencies the uncertainty produced by this distance may explain the deviation in the diffraction patterns shown in Figs. 26(d) and 27(d). At the highest frequency presented, the acoustic wavelength is within an order of magnitude of the horn diameter. Thus, the source cannot be approximated as a point source, and also likely contains a non-uniform directivity pattern. Table 3 describes the range of frequencies and their acoustic wavelength ratios relative to the diameter of the tapered horn.

Table 3. Predictions and measured point source conditions.

f (Hz)	kW	k (m^{-1})	λ (m)	D_T/λ
1000	9	18	0.35	0.02
2000	18	36	0.17	0.04
4000	37	74	0.09	0.07
8000	73	146	0.04	0.16
12000	110	220	0.03	0.22

Predictions using various point source locations within the diameter of the horn source are examined to assess the sensitivity of the source placement. The simulated source placement is varied along the x-axis from $-0.5D_T$ to $0.5D_T$. Figure 29 shows the diffraction pattern in the shadow zone for source locations at 8 and 12 kHz. Varying the source location on the x-axis by one half horn diameter significantly shifts the diffraction pattern. At 8 kHz the location of the maxima and minima are phase shifted for each source location. A consistent 2-3 dB difference is observed in magnitude due to the phase shift. The diffraction pattern from $-D_T/2$ to $D_T/2$ is symmetric about $\theta = 0$ deg. because of inherent symmetry. At 12 kHz the diameter of the horn tip is approximately a quarter of a wavelength and the diffraction pattern shifts if the source is moved $D_T/2$ in either direction. A full D_T displacement in source location results in a pattern that is phase shifted with large deviations (> 6 dB) in magnitude relative to measurement. Frequencies with wavelengths comparable to the radius of the horn result in a phase shifted diffraction pattern. The sensitivity of the diffraction pattern to the simulated source location can explain some of the disagreement observed relative to measurement at high frequencies.

The ray tracing method consistently under-predicts the shielding of the square edge plate and demonstrates improved agreement for the sharp edge plate relative to measurement. The FSC predictions are superior for the square edge case at higher frequencies, although the ray tracing predictions are within the same approximate dB error range at lower frequencies. Recall, both the present theory and FSC are not formulated for square edge geometries. The ray traced predictions show the largest discrepancies at the lowest frequency and in regions near the edge of the shadow zone. A Helmholtz number of $kW \approx 9$ is identified as a low frequency limit. Predictions of the diffracted field from a source varied within the finite distance of the horn diameter show the diffraction pattern is sensitive within the diameter at high frequencies. Despite the discrepancies relative to measurement, the ray tracing method is capable of predicting the correct trends of the diffraction pattern in the shielded region.
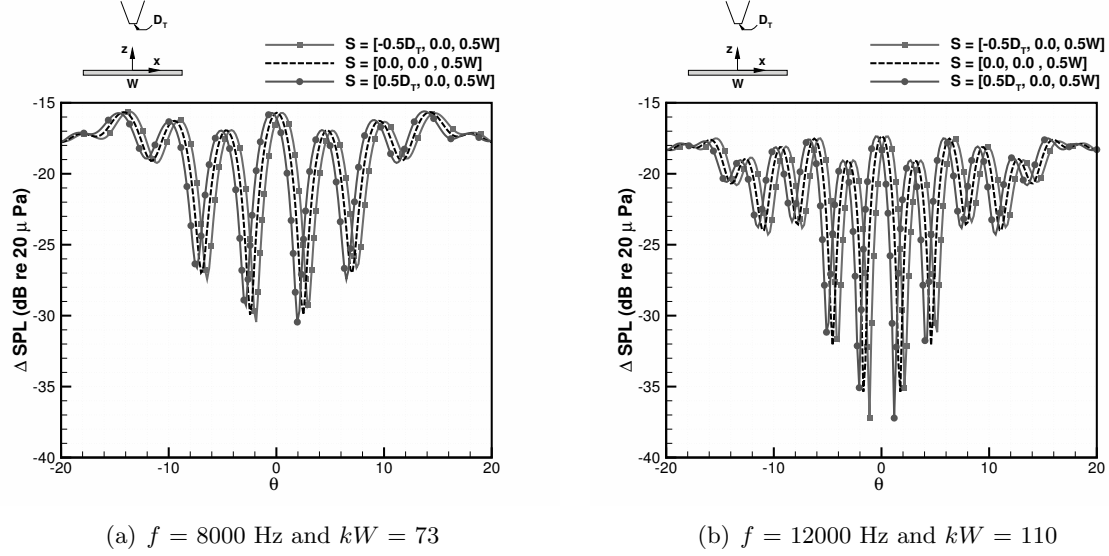
(a) $f = 8000$ Hz and $kW = 73$ (b) $f = 12000$ Hz and $kW = 110$

Figure 29. Source location sensitivity at high frequencies.

5   Predictions Compared with the NASA Jet-Surface Interaction Test (JSIT)

In this section, an assessment of the developed acoustic analogy combined with the ray tracing approach for the mixing component of jet noise in the presence of a scattering surface is presented. Measured data from the Jet-Surface Interaction Test (JSIT) of Brown et al. [54] are used to validate the predictions of jets disturbed by flat plates. The multi-phase experiment performed at NASA Glenn Research Center was intended to support researchers developing aircraft noise prediction tools by supplying data for a wide range of surface geometries, positions, and jet conditions. The first phase of the measurement involved capturing far-field noise from a jet near a simple planar surface with varying positions relative to the nozzle exit. A flat plate mounted on a two-axis traverse was used to simulate a shield or reflecting surface between the jet plume and the observer.

Comparisons with the shielded measurements are used to validate the developed model. The surface was moved through axial positions $2 < x_p/D < 20$ and radial positions $-1 < y_p/D < -10$. Recall, x_p is the axial distance from the nozzle exit to the trailing edge and y_p is the distance from the jet centerline to the plate surface. The exit diameter of the SMC series nozzles is $D = 0.0508$ m. The plate positions are illustrated in Fig. 30. In the measurement, the span of the plate is $100D$ and the nozzle centerline is in the middle. Also, in the measurement the edge of the plate in the sideline and upstream direction are covered with welding blankets. The plate was made of aluminum and was 0.0127 m thick with a 0.00635 m trailing edge angled at $\beta = 320.8$ deg. The far-field noise data were acquired from an azimuthal array of 24 microphones centered on the nozzle exit with a constant radius of 3.81 m ($75D$). The microphones were distributed along the arc at 5 deg. intervals ranging from $\Psi = 50$ deg. to 165 deg. relative to the jet upstream axis. The angles are illustrated in Fig. 30. A photograph of the experiment is shown in Fig. 31. Predictions are compared at various angles on the microphone arc. The range of experimental data used to validate the prediction model includes the plate configurations shown in Table 1 and the jet operating conditions shown in Table 2. The measured data are processed to account for atmospheric absorption (see Bass et al. [88, 89] for details) and corrected to a propagation distance

of $100D$.

Measurements have also been conducted by Bridges and Brown [90] for the same jet conditions but without the flat plate geometry. These are used to illustrate the prediction capability for free jets and the relative differences between the shielded predictions and measurements. Results are presented as Sound Pressure Level (SPL) per unit St, where $St = fD_j/u_j$ is the Strouhal number, and D_j and u_j are the fully expanded jet diameter and fully expanded velocity respectively. In the notation presented, Small Hot Jet Acoustic Rig (SHJAR) refers to measurements of the free jet and JSIT refers to the installed jet.
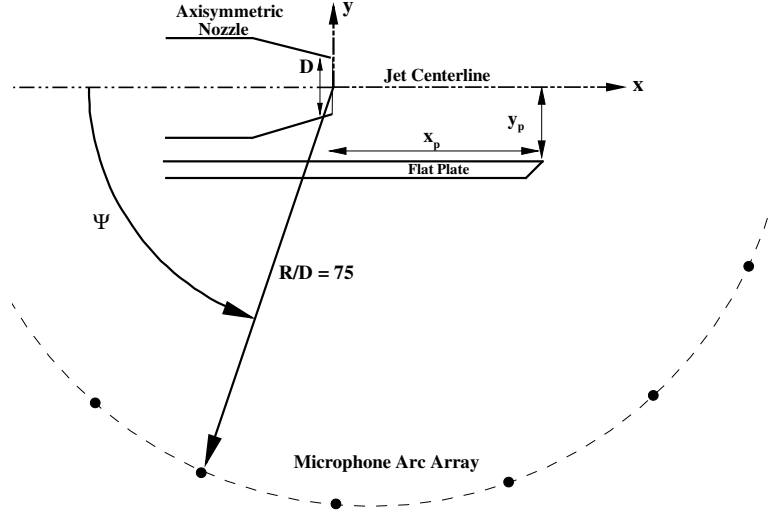
Figure 30. Coordinate system of the JSIT.

The first comparisons are shown in Fig. 32 for a jet operating at $M_j = 0.678$ and TTR $= 1.926$ from the SMC000 nozzle. The plate is located at $x_p/D = 10$ and $y_p/D = -2$. The predictions at observer angles $\Psi = 50$, 90, 110, and 150 deg. from the upstream jet axis are shown. The last information displayed in Fig. 32 is the parameter Γ calculated from the jet condition and plate location. All the following figures use this convention. At $\Psi = 50$ deg. in Fig. 32, the free jet prediction matches the experiment. The installed jet prediction and measurement both have a high frequency decay beginning at $St \approx 0.3$. At $\Psi = 90$ deg., the free jet prediction deviates from experiment at higher frequencies; however, the relative decrease in SPL from the shielding prediction agrees with the experiment. The installed jet prediction and measurement show a maximum decrease of 24 dB relative to the free jet prediction and measurement respectively at $St \approx 10$. At the downstream angle, $\Psi = 110$ deg., the maximum predicted shielding also agrees well with the experiment. The free jet prediction shows larger deviations at lower frequencies (6 to 8 dB). There is no predicted attenuation at $\Psi = 150$ deg. at high St, but the measurement shows a 8 to 10 dB decrease of SPL. For all observer angles, the maximum shielding for both the prediction and measurement occurs at the highest frequency. Jet structure interaction noise is present at lower frequencies, which is alluded to by the large value of $\Gamma = 0.469$. Recall, the developed prediction method accounts only for the jet mixing noise. Apart from the deviation in the lower frequency range where the additional noise sources dominate, the shielded predictions agree well with the experiment at all observer angles except downstream at $\Psi = 110$ and 150 degs. At $\Psi = 50$ and

90 degs., the predicted shielding is within ± 4 dB of the measurement above the peak jet mixing noise frequency. The prediction agrees within ± 6 dB of the experiment at $\Psi = 110$ deg. There is insignificant predicted shielding at the highest downstream angle of $\Psi = 150$ deg.

A second comparison is shown in Fig. 33 for the same jet condition but with the plate located at $x_p/D = 20$ and $y_p/D = -2$. There are additional sources present in the measurement due to jet structure interaction noise. This is predicted by the larger value of $\Gamma = 0.994$. However, there is less noise intensity increase at low frequencies compared to the $x_p/D = 10$ case. At frequencies higher than those of jet structure interaction noise, the prediction agrees within ± 2 dB of the experiment at the upstream and sideline observer angles. The prediction is also in better agreement with the measurement at the downstream angles relative to other plate configurations. At $\Psi = 130$ deg., the prediction is within ± 4 dB of the measurement. In contrast with the previous two plate locations, the shielding is captured by the prediction method at $\Psi = 150$ deg. The high frequency decay occurs at a higher cut-off frequency, $St \approx 0.2$, relative to experiment, $St \approx 0.1$, but the attenuation is within ± 4 dB at frequencies $St > 1$.

In Fig. 34, comparisons are presented for a trailing edge position of $x_p/D = 20$ and $y_p/D = -6$. Similar agreement is observed relative to the case with the surface located at $y_p/D = -2$, except at $\Psi = 150$ deg. At $\Psi = 50$ and 90 degs. there is strong agreement at high frequencies within ± 2 dB. The predicted attenuation rate at frequencies greater than the peak frequency matches the measurement at all angles except $\Psi = 150$ deg. There is no predicted shielding at the downstream angle $\Psi = 150$ deg. In contrast to the $y_p/D = -2$ case, the value of $\Gamma = 0.09$ is low and there is only a small region at low frequencies where there is an increase in noise. These comparisons display the trends for all plate locations listed in Table 1. The predictions of the cold subsonic $M_j = 0.985$ jet also follow the same trends and show the same relative agreement as with the $M_j = 0.678$ comparisons.

We now turn our attention to supersonic jets. Figure 35 shows spectra from a cold on-design $M_j = 1.5$ jet from the SMC016 nozzle with the plate located at $x_p/D = 20$ and $y_p/D = -2$. There is significantly less shielding for this plate configuration compared to the equivalent subsonic case. When the potential core length extends further downstream from the nozzle exit, there is a larger distribution of equivalent sources past the trailing edge of the plate that are not shielded. The jet operating condition and plate location result in $\Gamma = 0.461$ and additional jet-surface interaction noise is observed. The predicted SPL of the shielded configuration approaches measurement as the frequency increases and the contribution of surface interaction noise diminishes. The deviation from the experiment decreases with increasing frequency to within ± 1 dB at observer angles $\Psi = 50$, 90, and 110 degs. At $\Psi = 150$ deg., the shielding is over-predicted by up to 6 dB. The maximum attenuation at $\Psi = 150$ deg. agrees with the measurement, although the high frequency decay occurs at a higher cut-off frequency, $St = 0.4$, than experiment, $St = 0.1$.

Predictions and measurements of spectra are shown in Fig. 36 for an over-expanded $M_j = 1.29$ jet from the SMC016 nozzle. The plate is located at $x_p/D = 20$ and $y_p/D = -2$. Since the jet is off-design, shocks are present in the jet plume and resulting screech tones and BBSAN are observed in the measurements. Although the predictions do not take shock-associated noise into account, agreement is observed in the relative attenuation of the turbulent mixing noise. Outside the frequency range affected by the BBSAN, the predicted shielding follows the same high frequency rate of attenuation at all observer angles except $\Psi = 150$ deg. At $\Psi = 150$ deg., the predicted attenuation begins at a higher cut-off frequency and has a larger attenuation rate. This jet condition and plate location result in $\Gamma = 0.602$, and additional noise from the surface interaction is observed in the measurement.

Though disagreement between prediction and measurement is observed for select conditions and observer angles, most of the jet conditions and plate positions examined show that the overall trends

are captured by prediction. The comparisons shown are representative of all plate configurations and jet conditions examined. We summarize the prediction capability for installed jet mixing noise as follows:

1. The comparisons show that the acoustic analogy and tailored Green's function provided by ray tracing are capable of correctly capturing trends in measurement.

2. The predictions show strong agreement at higher frequencies. This is due to the use of ray tracing.

3. The predictions show strong agreement for large x_p/D, especially at upstream and sideline observer angles.

4. The prediction method captures the decrease in shielding effectiveness as the jet exit velocity increases.
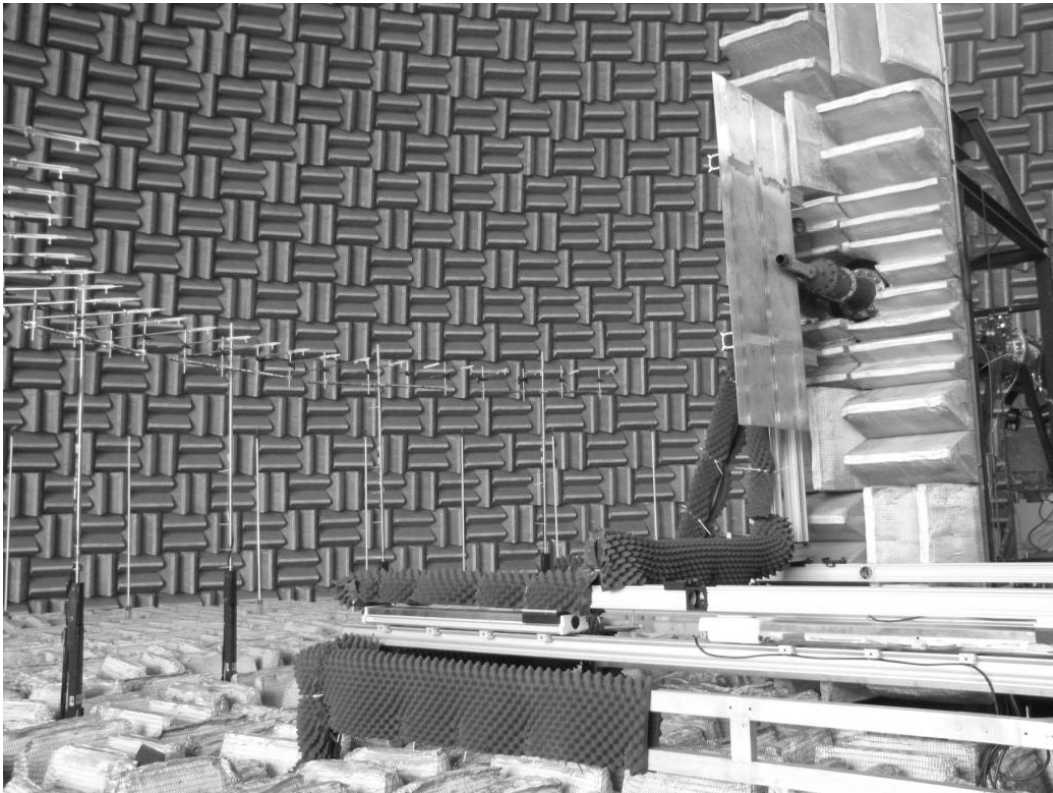
Figure 31.   A photograph of the jet structure interaction test courtesy of Podboy [87].
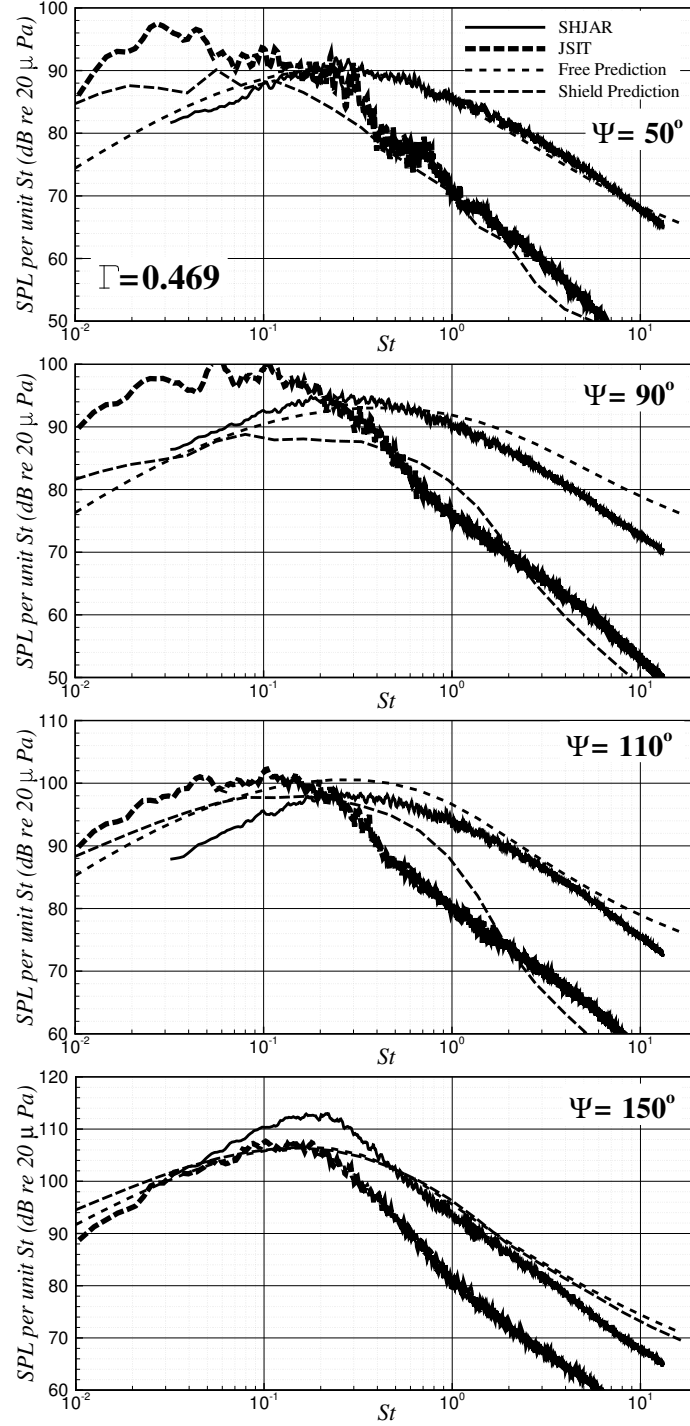
Figure 32. The free and installed jet predictions compared with measurements. The jet operates at $M_j = 0.678$ and TTR $= 1.926$ from the SMC000 nozzle with $D = 0.0508$ m and observers at $R/D = 100$. The plate is located at $x_p/D = 10$ and $y_p/D = -2$. These conditions result in $\Gamma = 0.469$.
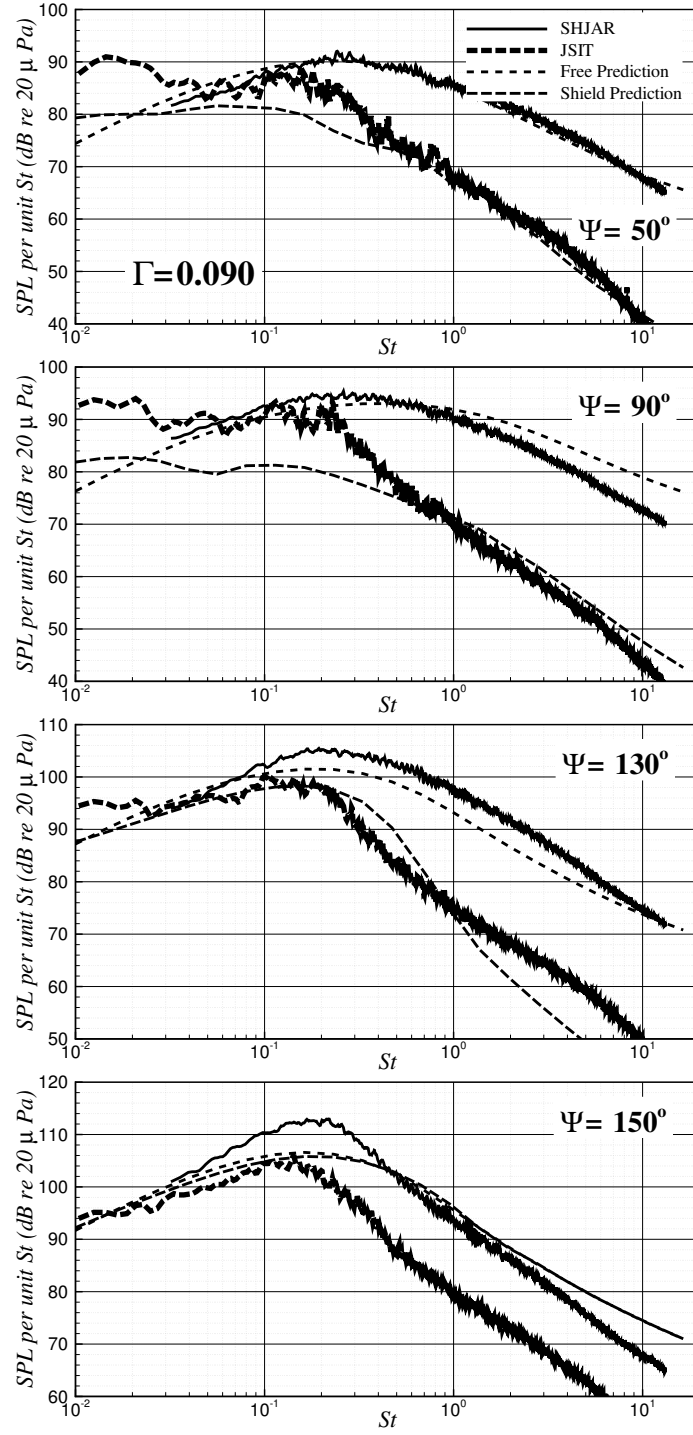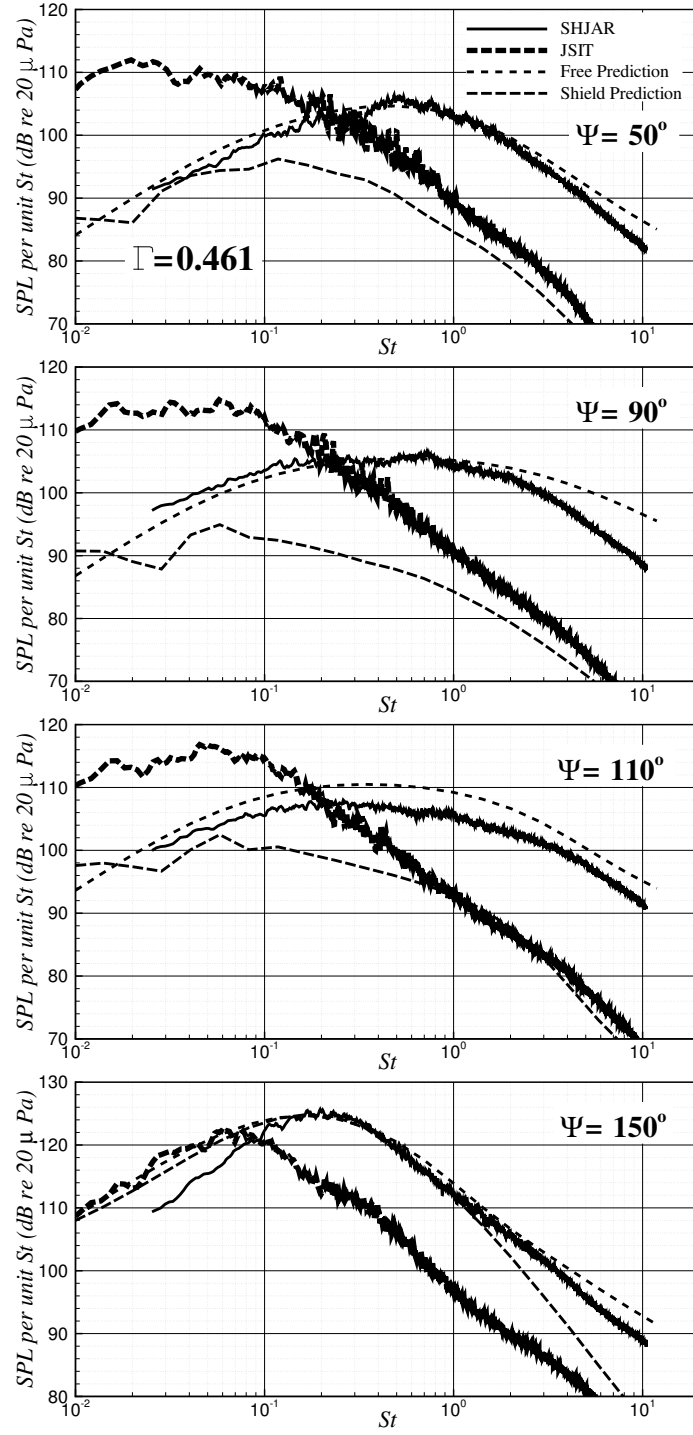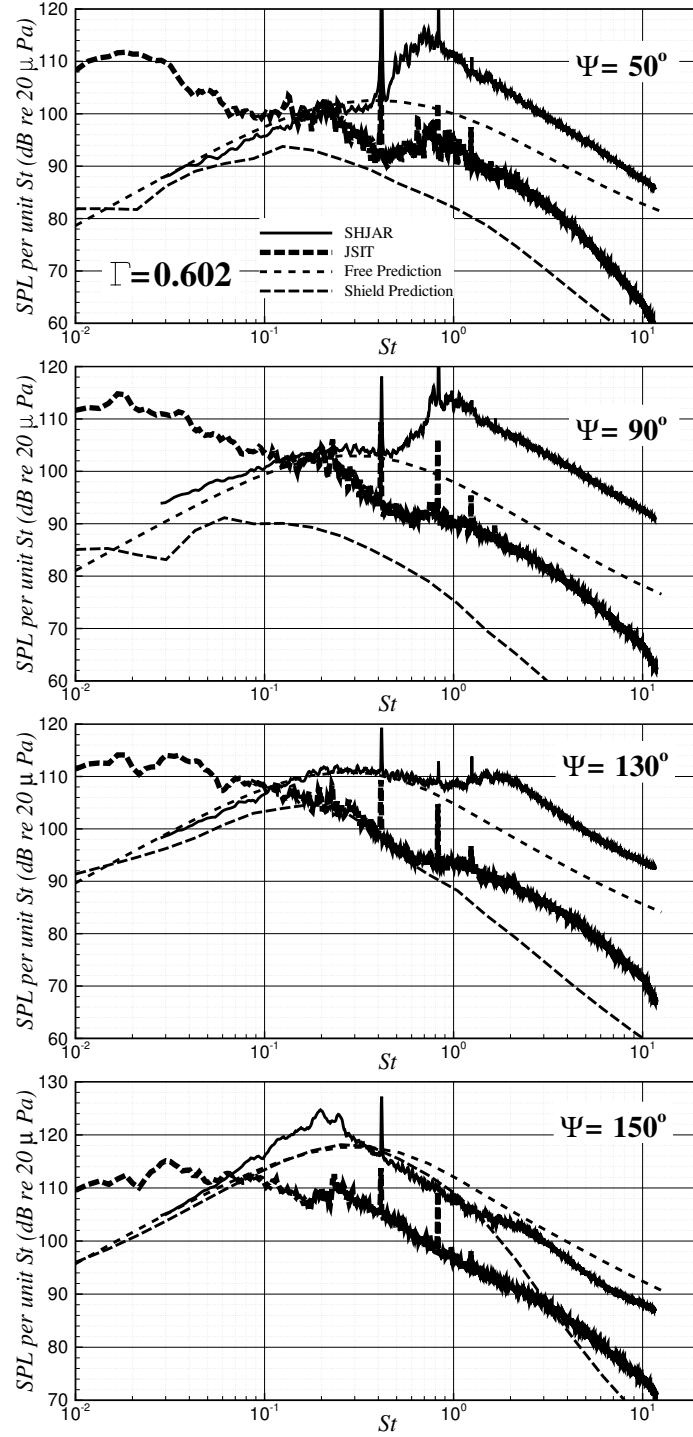
43
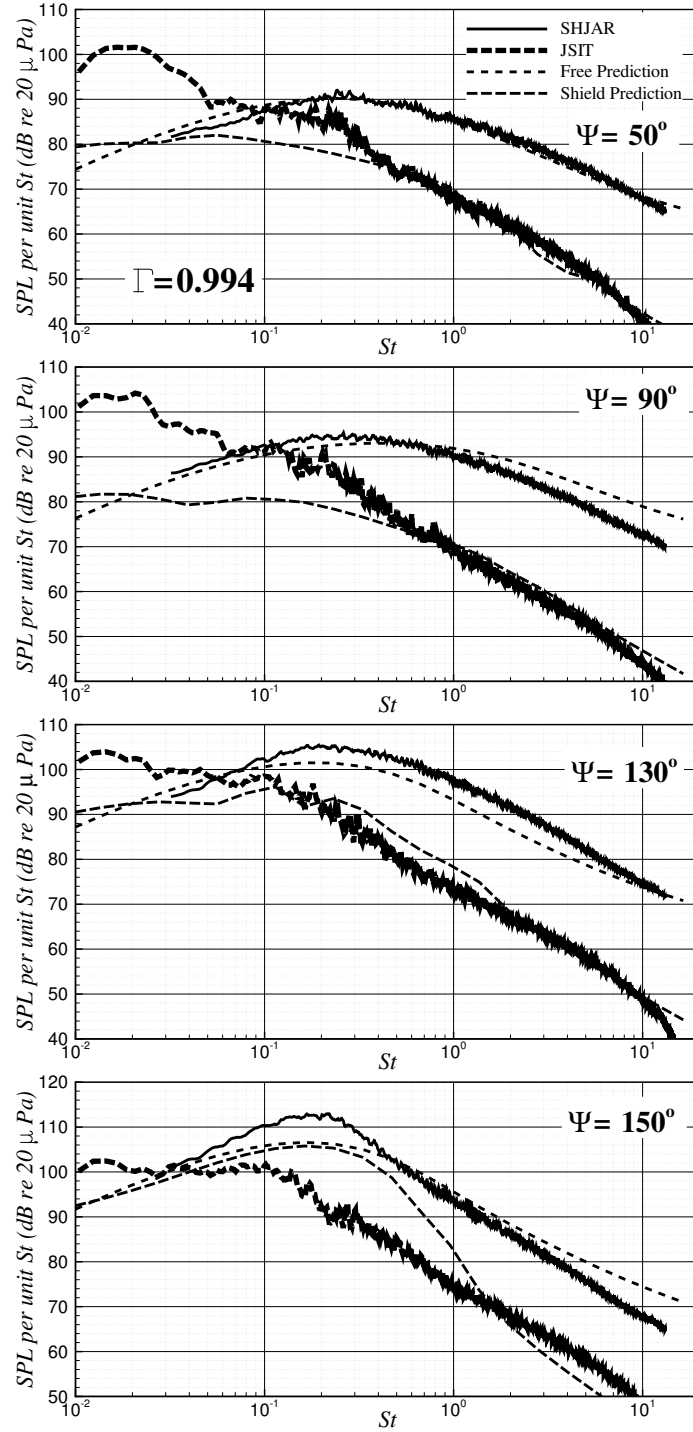
Figure 33. The free and installed jet predictions compared with measurements. The jet operates at $M_j = 0.678$ and TTR $= 1.926$ from the SMC000 nozzle with $D = 0.0508$ m and observers at $R/D = 100$. The plate is located at $x_p/D = 20$ and $y_p/D = -2$. These conditions result in $\Gamma = 0.994$.

Figure 34. The free and installed jet predictions compared with measurements. The jet operates at $M_j = 0.678$ and TTR = 1.185 from the SMC000 nozzle with $D = 0.0508$ m and observers at $R/D = 100$. The plate is located at $x_p/D = 20$ and $y_p/D = -6$. These conditions result in $\Gamma = 0.090$.

45

Figure 35. The free and installed jet predictions compared with measurements. The jet operates at $M_j = 1.50$ and TTR = 1.00 from the SMC016 nozzle with $D = 0.0508$ m and observers at $R/D = 100$. The plate is located at $x_p/D = 20$ and $y_p/D = -2$. These conditions result in $\Gamma = 0.461$.

Figure 36. The free and installed jet predictions compared with measurements. The jet operates at $M_j = 1.29$ and TTR $= 1.00$ from the SMC016 nozzle with $D = 0.0508$ m and observers at $R/D = 100$. The plate is located at $x_p/D = 20$ and $y_p/D = -2$. These conditions result in $\Gamma = 0.602$.

6 Summary and Conclusion

We have presented a new approach for predicting the scattering of jet mixing noise about airframe surfaces. The method is based on an acoustic analogy that involves the vector Green's function of the LEE and the source based on steady RANS solutions. The vector Green's function is written in terms of the Green's function of the convective wave equation. This latter Green's function is found numerically with a ray tracing approach. Aerodynamic statistics of free and installed jets are validated with PIV measurement and the predicted far-field noise is compared with microphone measurement. The combination of the developed theory, ray tracing, and careful implementation in a stand-alone computer program result in an approach that is more first principles than alternatives, numerically efficient, and captures the relevant physics of fluid-structure interaction and airframe geometry.

A non-dimensional number, Γ, is proposed that is used as a basic guide to determine if the aerodynamic source is affected by the airframe relative to the equivalent isolated jet aerodynamic source. The critical value of Γ predicts the on-set of jet structure interaction noise and when the jet deforms due to the presence of the airframe.

We summarize the comparisons of prediction with measurement and the theory with the following conclusions.

Aerodynamic Analysis

1. The aerodynamic assessment shows that nearby solid surfaces change the aerodynamic characteristics of the jet flow-field, even if the jet centerline is multiple diameters from a solid surface.

2. The effect of the airframe surface on the jet aerodynamics increases dramatically as the airframe approaches the nozzle axis and as the trailing edge extends further downstream.

Unsteady Aerodynamic Noise Source Analysis

1. Changes within the aerodynamic flow-field due to the presence of the airframe have a direct effect on the unsteady aerodynamic noise source.

2. The overall jet mixing noise intensity is decreased as the effective impingement surface area of the airframe is increased.

3. Γ is used as a guide to determine the on-set of jet structure interaction noise.

Jet-Surface Shielding Analysis

1. The ray traced predictions are validated with measurement and predict the correct trends of diffraction in the shadow region over a wide range of frequencies.

2. Predictions of scattered jet mixing noise are validated with measured data and capture the correct trends relative to jet operating conditions and airframe position.

References

1. Hill, G. and Thomas, R. H., "Challenges and Opportunities for Noise Reduction Through Advanced Aircraft Propulsion Airframe Integration and Configurations," *8th CEAS Workshop: Aeroacoustics of New Aircraft and Engine Configurations, November 11-12, Budapest, Hungary*, 2004.

2. Envia, E. and Thomas, R., "Emerging Community Noise Reduction Approaches," *3rd AIAA Atmospheric Space Environments Conference, June 27-30, Honolulu, Hawaii, AIAA Paper 2011-3532*, 2011. doi:10.2514/6.2011-3532.

3. Thomas, R. H., Burley, C. L., and Olson, E. D., "Hybrid Wing Body Aircraft System Noise Assessment with Propulsion Airframe Aeroacoustic Experiments," *16th AIAA/CEAS Aeroacoustics Conference, Stockholm, Sweden, 7 - 9 June, AIAA Paper 2010-3913*, 2010. doi:10.2514/6.2010-3913.

4. Czech, M. J., Thomas, R. H., and Elkoby, R., "Propulsion Airframe Aeroacoustic Integration Effects for a Hybrid Wing Body Aircraft Configuration," *16th AIAA/CEAS Aeroacoustics Conference, Stockholm, Sweden, 7 - 9 June, AIAA Paper 2010-3912*, 2010. doi:10.2514/6.2010-3912.

5. Horne, W. C. and Burnside, N. J., "AMELIA CESTOL Test: Acoustic Characteristics of Circulation Control Wing and Leading- and Trailing-Edge Slot Blowing," *51st AIAA Aerospace Sciences Meeting, January 7-10, Grapevine, Texas, AIAA Paper 2013-0978*, 2013. doi:10.2514/6.2013-978.

6. Welge, H. R., Nelson, C., and Bonet, J., "Supersonic Vehicle Systems for the 2020 to 2035 Timeframe," *28th AIAA Applied Aerodynamics Conference, Chicago, Illinois, June 28 - July 1, AIAA Paper 2010-4930*, 2010. doi:10.2514/6.2010-4930.

7. Welge, H. R., Bonet, J., Magee, T., Chen, D., Hollowell, S., Kutzmann, A., Mortlock, A., Stengle, J., Nelson, C., Adamson, E., Baughcum, S., Britt, R. T., Miller, G., and Tai, J., "N+2 Supersonic Concept Development and Systems Integration," *NASA/CR 2010-216842*, 2010.

8. Morgenstern, J. M., Stelmach, M., and Jha, P. D., "Advanced Concept Studies for Supersonic Commercial Transports Entering Service in 2030-35 (N+3)," *28th AIAA Applied Aerodynamics Conference, Chicago, Illinois, June 28 - July 1, AIAA Paper 2010-5144*, 2010. doi:10.2514/6.2010-5114.

9. Sokhey, J. S. and Kube-McDowell, M., "Low Noise Highly Variable Cycle Nozzle for Next Generation Supersonic Aircraft," *NASA ARMD Fundamental Aeronautics Program Technical Conference*, 2008.

10. Paliath, U. and Premasuthan, S., "Physics of Turbulent Flow," *19th AIAA/CEAS Aeroacoustics Conference, AIAA Paper 2013-2137*, 2013. doi:10.2514/6.2013-2137.

11. Bogey, C. Bailly, C. and Juve, D., "Noise Investigation of a High Subsonic, Moderate Reynolds Number Jet using a Compressible LES," *Theoretical and Computational Fluid Dynamics*, Vol. 16, No. 4, 2003, pp. 273–297. doi:10.1007/s00162-002-0079-4.

12. Papamoschou, D. and Mayoral, S., "Jet Noise Shielding for Advanced Hybrid Wing-Body Configurations," *49th AIAA Aerospace Sciences Meeting, AIAA Paper 2011-912*, 2011. doi:10.2514/6.2011-912.

13. Freund, J. B., Lele, S. K., and Moin, P., "Numerical Simulation of a Mach 1.92 Turbulent Jet and its Sound Field," *AIAA*, Vol. 38, No. 11, 2000, pp. 2023–2031. doi:10.2514/2.889.

14. Miller, S. A. E., "Toward a Comprehensive Model of Jet Noise using an Acoustic Analogy," *AIAA Journal*, 2014. doi:10.2514/1.J052809.

15. Mollo-Christensen, E., "Physics of Turbulent Flow," *AIAA Journal*, Vol. 9, No. 7, 171, pp. 1217–1228. doi:10.2514/3.49933.

16. Tam, C. K. W., Golebiowski, M., and Seiner, J. M., "On the Two Components of Turbulent Mixing Noise from Supersonic Jets," *2nd AIAA/CEAS Aeroacoustics Conference, State College, Pennsylvania, May 6-8, AIAA Paper 1996-1716*, 1996. doi:10.2514/6.1996-1716.

17. Viswanathan, M., "Analysis of the Two Similarity Components of Turbulent Mixing Noise," *AIAA*, Vol. 40, No. 9, 2002, pp. 1735–1744. doi:10.2514/2.1878.

18. Tam, C. K. W., "Supersonic Jet Noise," *Annual Review of Fluid Mechanics*, Vol. 27, 1995, pp. 17–43. doi:10.1146/annurev.fl.27.010195.000313.

19. Tam, C. K. W. and Auriault, L., "Jet Mixing Noise from Fine-Scale Turbulence," *AIAA Journal*, Vol. 37, No. 2, 1999, pp. 145–153. doi:10.2514/2.691.

20. Morris, P. J. and Farassat, F., "Acoustic Analogy and Alternative Theories for Jet Noise Prediction," *AIAA Journal*, Vol. 40, No. 4, 2002, pp. 671–680. doi:10.2514/2.1699.

21. Ffowcs Williams, J. E. and Hawkings, D. L., "Sound Generation by Turbulence and Surfaces in Arbitrary Motion," *Philosophical Transactions of the Royal Society A: Mathematical, Physical and Engineering Sciences*, Vol. 264, No. 1151, 1969, pp. 321–342. doi:10.1098/rsta.1969.0031.

22. Ffowcs Williams, J. E., "Aeroacoustics," *Annual Review of Fluid Mechanics*, Vol. 9, 1977, pp. 447–68. doi:10.1146/annurev.fl.09.010177.002311.

23. Goldstein, M. E., "Aeroacoustics of Turbulent Shear Flows," *Annual Review of Fluid Mechanics*, Vol. 16, 1984, pp. 263–285. doi:10.1146/annurev.fl.16.010184.001403.

24. Harper-Bourne, M. and Fisher, M. J., "The Noise from Shock-Waves in Supersonic Jets," AGARD Conference Proceedings, 1973.

25. Tam, C. K. W., "Stochastic Model Theory of Broadband Shock-Associated Noise from Supersonic Jets," *Journal of Sound and Vibration*, Vol. 116, No. 2, 1987, pp. 265–302. doi:10.1016/S0022-460X(87)81303-2.

26. Tam, C. K. W., "Broadband Shock-Associated Noise of Moderately Imperfectly-Expanded Supersonic Jets," *Journal of Sound and Vibration*, Vol. 140, No. 1, 1990, pp. 55–71. doi:10.1016/0022-460X(90)90906-G.

27. Morris, P. J. and Miller, S. A. E., "The Prediction of Broadband Shock-Associated Noise using RANS CFD," 15th AIAA/CEAS Aeroacoustics Conference (30th AIAA Aeroacoustics Conference), AIAA Paper 2009-3315, 2009.

28. Powell, A., "On the Noise Emanating from a Two-Dimensional Jet above the Critical Pressure," *Aeronautical Quarterly*, Vol. 4, 1953, pp. 103–122.

29. Raman, G., "Supersonic Jet Screech: Half-Century from Powell to the Present," *Journal of Sound and Vibration*, Vol. 222, No. 3, 1999, pp. 543–571. doi:10.1006/jsvi.1999.2181.

30. Sawyer, R. A., "Two-dimensional Reattaching Jet Flows Including the Effects of Curvature on Entrainment," *Journal of Fluid Mechanics*, Vol. 17, 1963, pp. 481–498. doi:10.1017/S0022112063001464.

31. Al-Qutub, A. M. and Budair, M. O., "Experiments on the Flow Over a Flat Surface Impinged by a Supersonic Jet," *31st AIAA/ASME/SAE/ASEE Joint Propulsion Conference and Exhibit, San Diego, California, 10 - 12 July, AIAA Paper 1995-2935*, 1995. doi:10.2514/6.1995-2935.

32. Donaldson, C. D. and Snedeker, R. S., "A Study of Free Jet Impingement. Part 1. Mean Properties of Free and Impinging Jets," *Journal of Fluid Mechanics*, Vol. 45, 1971, pp. 281–319. doi:10.1017/S0022112071000053.

33. Lamont, P. J. and Hunt, B. L., "The Impingement of Underexpanded, Axisymmetric Jets on Perpendicular and Inclined Flat Plates," *Journal of Fluid Mechanics*, Vol. 100, 1980, pp. 471–511. doi:10.1017/S0022112080001255.

34. Miller, S. A. E., "The Prediction of Noise due to Jet Turbulence Convecting past Flight Vehicle Trailing Edges," *AIAA Aviation and Aeronautics Forum and Exposition (20th AIAA/CEAS Aeroacoustics Conference), Atlanta, Georgia, June 16-20, AIAA Paper 2014-2341*, 2014. doi:10.2514/6.2014-2341.

35. Curle, G. M., "The Influence of Solid Boundaries upon Aerodynamic Sound," *Proceedings of the Royal Society A: Mathematical, Physical and Engineering Sciences*, Vol. 231, No. 1187, 1955, pp. 505–514. doi:10.1098/rspa.1955.0191.

36. Ffowcs Williams, J. E. and Hall, L. H., "Aerodynamic Sound Generation by Turbulent Flow in the Vicinity of a Scattering Half Plane," *Journal of Fluid Mechanics*, Vol. 40, 1970, pp. 657–670. doi:10.1017/S0022112070000368.

37. Crighton, D. G. and Lippington, F. G., "Scattering of Aerodynamic Noise by a Semi-infinite Compliant Plate," *Journal of Fluid Mechanics*, Vol. 43, No. 4, 1970, pp. 721–736. doi:10.1017/S0022112070002690.

38. Amiet, R. K., "Noise Due to Turbulent Flow Past a Trailing Edge," *Journal of Sound and Vibration*, Vol. 47, No. 3, 1976, pp. 387–393. doi:10.1016/0022-460X(76)90948-2.

39. Lighthill, M. J., "On Sound Generated Aerodynamically: I. General Theory," *Proceedings of the Royal Society of London*, Vol. 211, 1952, pp. 564–587. doi:10.1098/rspa.1952.0060.

40. Lighthill, M. J., "On Sound Generated Aerodynamically: II. Turbulence as a Source of Sound," *Proceedings of the Royal Society of London*, Vol. 222, 1954, pp. 1–32. doi:10.1098/rspa.1954.0049.

41. Lilley, G. M., "On the Noise from Jets," *AGARD Conference Proceedings In Noise Mechanisms*, Vol. 13, 1974, pp. 1–11.

42. Khavaran, A., Krejsa, E. A., and Kim, C. M., "Computation of Supersonic Jet Mixing Noise for an Axisymmetric Convergent-Divergent Nozzle," *Journal of Aircraft*, Vol. 31, No. 3, 1994, pp. 603–609. doi:10.2514/3.46537.

43. Mani, R., Stringas, E. J., Wang, J. C. F., Balsa, T. F., Gliebe, P. R., and Kantola, R. A., "High Velocity Jet Noise Source Location and Reduction," *FAA-RD-76-79-II*, 1977.

44. Morris, P. J. and Boluriaan, S., "The Prediction of Jet Noise From CFD Data," *10th AIAA/CEAS Aeroacoustics Conference, Manchester, Great Britain, May 10-12, AIAA Paper 2004-2977*, 2004. doi:10.2514/6.2004-2977.

45. Huang, C. and Papamoschou, D., "Numerical Study of Noise Shielding by Airframe Structures," *14th AIAA/CEAS Aeroacoustics Conference, Vancouver, British Columbia Canada, 5 - 7 May, AIAA Paper 2008-2999*, 2008. doi:10.2514/6.2008-2999.

46. Agarwal, A. and Dowling, A. P., "The Calculation of Acoustic Shielding of Engine Noise by the Silent Aircraft Airframe," *11th AIAA/CEAS Aeroacoustics Conference, Monterey, California, 23 - 25 May, AIAA Paper 2005-2996*, 2005. doi:10.2514/6.2005-2996.

47. Dunn, M. H. and Tinetti, A. F., "Aeroacoustic Scattering Via The Equivalent Source Method," *10th AIAA/CEAS Aeroacoustics Conference, AIAA Paper 2004-2937*, 2004. doi:10.2514/6.2004-2937.

48. Tinetti, A. F., Dunn, M. H., and Pope, S., "Fast Scattering Code (FSC) User's Manual, Version 2.0," *NASA/CR 2006-214510*, Oct. 2006.

49. Tinetti, A. F. and Dunn, M. H., "The Fast Scattering Code (FSC): Validation Studies and Program Guidelines," *NASA/CR-2011-217158*, 2011.

50. Agarwal, A., Dowling, A. P., and Graham, W., "A Ray Tracing Approach to Calculate Acoustic Shielding by the Silent Aircraft Airframe," *12th AIAA/CEAS Aeroacoustics Conference, Cambridge, Massachussetts, 8 - 10 May, AIAA Paper 2006-2618*, 2006. doi:10.2514/6.2006-2618.

51. Miller, S. A. E., "The Prediction of Jet Noise Ground Effects using an Acoustic Analogy and a Tailored Green's Function," *Journal of Sound and Vibration*, Vol. 333, No. 4, 2014, pp. 1193–1207. doi:10.1016/j.jsv.2013.10.028.

52. Bridges, J. and Wernet, M. P., "The NASA Subsonic Jet Particle Image Velocimetry (PIV) Dataset," *NASA/TM-2011-216807*, 2011.

53. Ahtye, W. and McCulley, G., "Evaluation of Approximate Methods for the Prediction of Noise Shielding by Airframe Components," *NASA/TP-1980-1004*, 1980.

54. Brown, C., "Jet-Surface Interaction Test: Far-Field Noise Results," *J. Eng. Gas Turbines Power*, Vol. 135, No. 7, 2011, pp. 7. doi:10.1115/1.4023605.

55. Morris, P. J. and Miller, S. A. E., "Prediction of Broadband Shock-Associated Noise Using Reynolds-Averaged Navier-Stokes Computational Fluid Dynamics," *AIAA*, Vol. 48, No. 12, 2010, pp. 2931–2944. doi:10.2514/1.J050560.

56. Tam, K. W., "Jet Noise: Since 1952," *Theoretical and Computational Fluid Dynamics*, Vol. 10, 1998, pp. 393–405. doi:10.1007/s001620050072.

57. Raizada, N., "Numerical Prediction of Noise from High Speed Subsonic Jets using an Acoustic Analogy," *M.S. Thesis The Pennsylvania State University*, December 2005.

58. Goldstein, M. E., "Aeroacoustics," McGraw-Hill International Book Company, New York, 1976.

59. Goldstein, M. E., "The Low Frequency Sound from Multipole Sources in Axisymmetric Shear Flows, with Applications to Jet Noise," *Journal of Fluid Mechanics*, Vol. 70, No. 3, 1975, pp. 595–604. doi:10.1017/S0022112075002212.

60. Goldstein, M. E., "The Low Frequency Sound from Multipole Sources in Axisymmetric Shear Flows - Part II," *Journal of Fluid Mechanics*, Vol. 75, No. 1, 1976, pp. 17–28. doi:10.1017/S0022112076000104.

61. Balsa, T. F., Gliebe, P. R., Kantola, R. A., Mani, R., and Stringas, E. J., "High Velocity Jet Noise Source Location and Reduction. Task 2. Theoretical Developments and Basic Experiments," *Defense Technical Information Center*, 1978.

62. Katsikadelis, J., *Boundary Elements: Theory and Applications*, Elsevier Science, 1st ed., 2002.

63. Liu, Y. J., "Fast Multipole Boundary Element Method - Theory and Applications in Engineerings," *Cambridge University Press, Cambridge*, 2009.

64. Keller, J. B., "Geometrical Theory of Diffraction," *Journal of the Optical Society of America*, Vol. 52, 1961, pp. 116–130.

65. Suzuki, T., "High-Frequency Acoustic Fields Solved Based on Geometrical Acoustics: Direct Waves, Reflected Waves, Creeping Waves, Diffracted Waves and Caustics," *16th AIAA/CEAS Aeroacoustics Conference, Stockholm, Sweden, 7 - 9 June, AIAA Paper 2010-3726*, 2010. doi:10.2514/6.2010-3726.

66. van Rens, J. R. P., van Rens, B. J. E., van Holten, T., and Ruijgrok, G. J. J., "Sound Level Prediction using a Ray Tracing Algorithm for a Blended Wing Body," *6th AIAA/CEAS Aeroacoustics Conference, Lahaina, HI, 12 - 14 June, AIAA Paper 2000-2069*, 2000. doi:10.2514/6.2000-2069.

67. Lummer, M., "Maggi-Rubinowicz Diffraction Correction for Ray-Tracing Calculations of Engine Noise Shielding," *14th AIAA/CEAS Aeroacoustics Conference, Vancouver, British Columbia Canada, 5 - 7 May, AIAA Paper 2008-3050*, 2008. doi:10.2514/6.2008-3050.

68. Kinsler, L., Frey, A. R., Coppens, A. B., and Sanders, J. V., *Boundary Elements: Theory and Applications*, John Wiley and Sons, Inc, 4th ed., 2000.

69. Pierce, A. D., *Acoustics: An Introduction to Physical Principles and Applications*, American Institute of Physics, 1994.

70. Sommerfeld, A., *Lectures on Theoretical Physics: Optics*, Vol. 4, Academic Press, Inc, 1964.

71. Levy, B. and Keller, J. B., "Diffraction by a Smooth Object," *Communications on Pure and Applied Mathematics*, Vol. 12, 1959, pp. 159–209.

72. Agarwal, A., Dowling, A. P., Shin, H.-C., Graham, W., and Sefi, S., "Ray-Tracing Approach to Calculate Acoustic Shielding by a Flying Wing Airframe," *AIAA Journal*, Vol. 45, No. 5, 2007, pp. 1080–1090. doi:10.2514/1.26000.

73. Keller, J. B., "Diffraction by an Aperture," *Journal of Applied Physics*, Vol. 28, No. 4, 1957, pp. 426–444.

74. Kraus, L. and Levine, L. M., "Diffraction by an Elliptic Cone," *Communications on Pure and Applied Mathematics*, Vol. 14, 1961, pp. 49–68.

75. Felsen, L. B., "Backscattering from Wide-Angle and Narrow-Angle Cones," *Journal of Applied Physics*, Vol. 26, No. 2, 1955, pp. 136–151.

76. Siegel, K. M., Crispen, J. W., and Schensted, C. E., "Electromagnetic and Acoustical Scattering from a Semi-Infinite Cone," *Journal of Applied Physics*, Vol. 26, No. 3, 1955, pp. 309–313. doi:10.1063/1.1721983.

77. Lau, J. C., "Effects of Exit Mach Number and Temperature on Mean-Flow and Turbulence Characteristics in Round Jets," *Journal of Fluid Mechanics*, Vol. 105, 1981, pp. 193–218. doi:10.1017/S0022112081003170.

78. Glassner, A. S., *An Introduction to Ray Tracing*, Academic Press, Inc, 1989.

79. "FUN3D Manual," *NASA Langley Research Center, Hampton, VA*, Aug. 2012, URL: http://fun3d.larc.nasa.gov/.

80. Menter, F. R., "Two-Equation Eddy-Viscosity Turbulence Models for Engineering Applications," *AIAA Journal*, Vol. 32, No. 8, 1994, pp. 1598–1605. doi:10.2514/3.12149.

81. Jones, W. P. and Launder, B. E., "The Prediction of Laminarization with a Two-Equation Model of Turbulence," *International Journal of Heat and Mass Transfer*, Vol. 15, 1972, pp. 301–314.

82. Wilcox, D. C. and Traci, R. M., "A Complete Model of Turbulence," *9th AIAA Fluid and Plasma Dynamics Conference, San Diego, California, 14 - 16 July, AIAA Paper 1976-351*, 1976. doi:10.2514/6.1976-351.

83. Wilcox, D. C., "A Half Century Historical Review of the k-ω Model," *29th AIAA Aerospace Sciences Meeting, Reno, Nevada, 7 - 10 January, AIAA Paper 1991-0615*, 1991. doi:10.2514/6.1991-615.

84. Georgiadis, N., Yoder, D. A., and Engblom, W. A., "Evaluation of Modified Two-Equation Turbulence Models for Jet Flow Predictions," *AIAA Journal*, Vol. 44, 2006. doi:10.2514/1.22650.

85. Thomas, R. H., Czech, M. J., and Doty, M. J., "High Bypass Ratio Jet Noise Reduction and Installation Effects Including Shielding Effectiveness," *51st AIAA Aerospace Sciences Meeting, Grapevine, Texas, 7 - 10 January, AIAA Paper 2013-0541*, 2013. doi:10.2514/6.2013-541.

86. Brooks, T. F., Humphreys, W. M., and Plassman, G. E., "DAMAS Processing for a Phased Array Study in the NASA Langley Jet Noise Laboratory," *16th AIAA/CEAS Aeroacoustics Conference, Stockholm, Sweden, 7 - 9 June, AIAA Paper 2010-3780*, 2010. doi:10.2514/6.2010-3780.

87. Podboy, G. G., "Jet-Surface Interaction Test: Phased Array Noise Source Localization Results," *Proceeding of the ASME Turbo Expo, Copenhagen, Denmark, June 14-18, GT2012-69801*, 2012.

88. Bass, H. E., Sutherland, L. C., Zuckerwar, A. J., Blackstock, D. T., and Hester, D. M., "Atmospheric Absorption of Sound: Further Developments," *Journal of the Acoustical Society of America*, Vol. 97, No. 1, 1995, pp. 680–683. doi:10.1121/1.412989.

89. Bass, H. E., Sutherland, L. C., Zuckerwar, A. J., Blackstock, D. T., and Hester, D. M., "Erratum: Atmospheric absorption of sound: Further developments," *Journal of the Acoustical Society of America*, Vol. 99, No. 2, 1996, pp. 1259–1259. doi:10.1121/1.415223.

90. Bridges, J. and Brown, C. A., "Validation of the Small Hot Jet Acoustic Rig for Aeroacoustic Research," *11th AIAA/CEAS Aeroacoustics Conference, Monterey, California, 23 - 25 May, AIAA Paper 2005-2846*, 2005. doi:10.2514/6.2005-2846.

REPORT DOCUMENTATION PAGE

1. REPORT DATE *(DD-MM-YYYY)*	2. REPORT TYPE	3. DATES COVERED *(From - To)*
01- 07 - 2014	Technical Memorandum	

4. TITLE AND SUBTITLE

The Prediction and Analysis of Jet Flows and Scattered Turbulent Mixing Noise About Flight Vehicle Airframes

5a. CONTRACT NUMBER

5b. GRANT NUMBER

5c. PROGRAM ELEMENT NUMBER

6. AUTHOR(S)

Miller, Steven A. E.

5d. PROJECT NUMBER

5e. TASK NUMBER

5f. WORK UNIT NUMBER

475122.02.07.05.01

7. PERFORMING ORGANIZATION NAME(S) AND ADDRESS(ES)

NASA Langley Research Center
Hampton, VA 23681-2199

8. PERFORMING ORGANIZATION REPORT NUMBER

L-20444

9. SPONSORING/MONITORING AGENCY NAME(S) AND ADDRESS(ES)

National Aeronautics and Space Administration
Washington, DC 20546-0001

10. SPONSOR/MONITOR'S ACRONYM(S)

NASA

11. SPONSOR/MONITOR'S REPORT NUMBER(S)

NASA/TM-2014-218506

12. DISTRIBUTION/AVAILABILITY STATEMENT

Unclassified - Unlimited
Subject Category 71
Availability: NASA CASI (443) 757-5802

13. SUPPLEMENTARY NOTES

14. ABSTRACT

Jet flows interacting with nearby surfaces exhibit a complex behavior in which acoustic and aerodynamic characteristics are altered. The physical understanding and prediction of these characteristics are essential to designing future low noise aircraft. A new approach is created for predicting scattered jet mixing noise that utilizes an acoustic analogy and steady Reynolds-averaged Navier-Stokes solutions. A tailored Green's function accounts for the propagation of mixing noise about the airframe and is calculated numerically using a newly developed ray tracing method. The steady aerodynamic statistics, associated unsteady sound source, and acoustic intensity are examined as jet conditions are varied about a large flat plate. A non-dimensional number is proposed to estimate the effect of the aerodynamic noise source relative to jet operating condition and airframe position.The steady Reynolds-averaged Navier-Stokes solutions, acoustic analogy, tailored Green's function, non-dimensional number, and predicted noise are validated with a wide variety of measurements. The combination of the developed theory, ray tracing method, and careful implementation in a stand-alone computer program result in an approach that is more first principles oriented than alternatives, computationally efficient, and captures the relevant physics of fluid-structure interaction.

15. SUBJECT TERMS

Acoustic analogy; Diffraction; Fluid-structure interaction; Green's function; Jet; Jet flow; Jet noise; Radiation; Ray theory; Shielding

16. SECURITY CLASSIFICATION OF:			17. LIMITATION OF ABSTRACT	18. NUMBER OF PAGES	19a. NAME OF RESPONSIBLE PERSON
a. REPORT	b. ABSTRACT	c. THIS PAGE			STI Help Desk (email: help@sti.nasa.gov)
U	U	U	UU	60	19b. TELEPHONE NUMBER *(Include area code)* (443) 757-5802